Available online at www.sciencedirect.com
SCIENCE DIRECT®
Journal of Computational Physics 197 (2004) 1–27
JOURNAL OF COMPUTATIONAL PHYSICS
www.elsevier.com/locate/jcp

A visual fluctuation splitting scheme for magnetohydrodynamics with a new sonic fix and Euler limit

Necdet Aslan

Physics Department, Yeditepe University, Kayışdağı, 81120 Istanbul, Turkey

Received 14 February 2003; received in revised form 18 November 2003; accepted 19 November 2003
Available online 9 April 2004

Abstract

This paper presents a two dimensional visual computer code developed to solve magnetohydrodynamic (MHD) equations. This code runs on structured and unstructured triangles and operates by a fluctuation splitting (FS) scheme. The FS scheme originally introduced by Roe [in: K.W. Morton, M.J. Baines (Eds.), Numerical Methods for Fluid Dynamics II, Academic Press, New York, 1982] to solve Euler equations was extended by Aslan [J. Comput. Phys. 153 (1999) 437] for solving ideal MHD equations. Aslan's method included a wave model, called MHD-A, consisting of slow and fast magneto-acoustic waves as well as an entropy and artificial magnetic monopole wave. In this work, Aslan's method was extended to include external sources, a new sonic fix, and a careful normalization in the Euler limit. It is shown by numerical experiments that VIS-MHD-A is able to work accurately for a wide range of problems including discontinuities, shock structures, and problems including smooth solutions (e.g., Rayleigh–Taylor and Kelvin–Helmholtz instability).

1. Introduction

Over the last few decades, the computational fluid dynamics (CFD) has offered numerous tools to scientists and engineers. It has played a major role in the design of complicated space vehicles, complex industrial machinery, safer nuclear plants, etc. CFD has also been an increasingly employed tool in a variety of fields such as nonlinear wave propagation, turbulence, aeroelastic interactions, and plasma interactions. High resolution numerical techniques in CFD are also being developed by plasma physicists to analyze astrophysical, fusion, and laboratory plasma flows all consisting of single or multispecies gases. In order to analyze such complicated systems in detail, it is better to visually follow the time (or iteration) evolution of the numerical solutions obtained by these schemes. The scientific visualization not only allows the investigator to follow the physical quantities in time but it also helps to determine the numerical inconsistencies near boundaries, discontinuities, stagnation points, etc., during the code development. In this

E-mail address: naslan@yeditepe.edu.tr (N. Aslan).

0021-9991/$ - see front matter © 2003 Elsevier Inc. All rights reserved.
doi:10.1016/j.jcp.2003.11.029

work, the detailed features of a new computer code (VIS-MHD-A) that works for challenging CFD problems are presented along with its user-friendly visualization capability. The efficient normalization of wave model, MHD-A in pure hydrodynamics (HD) limit (with vanishing magnetic field) and a new sonic fix that eliminates unphysical expansion shocks (based on the correct sonic gradient idea introduced in [3]) are the new features of this wave model. In addition, the new scheme is able to run under the effects of external fields, including gravitational field. This new version of the computer code called VIS-MHD-A also includes a user-friendly visualization capability to provide an interactive usage for educational or parallel processing purposes [4]. All the plots presented in this work were obtained by taking screen snapshots produced by this code. This new robust and accurate code allows a thorough investigation of steady or transient solutions of two dimensional HD or MHD equations on structured or unstructured triangular meshes.

2. The MHD equations

The set of two dimensional ($\partial/\partial z \equiv 0$, $B_z = 0$, $V_z = 0$) planar MHD equations in Cartesian geometry is given by the following conservative form:

$$\frac{\partial \mathbf{U}}{\partial t} + \frac{\partial}{\partial x}[\mathbf{F}(\mathbf{U})] + \frac{\partial}{\partial y}[\mathbf{G}(\mathbf{U})] = \mathbf{S}, \tag{1}$$

where $\mathbf{S}$ is the source including external as well as artificial monopole and sonic sources (Section 2.4) and $\mathbf{U} = (\rho, \rho V_x, \rho V_y, B_x, B_y, E)^{\mathrm{T}}$ is the conservative state vector of fluid variables (with ρ: density, $\rho\mathbf{V}$: momentum, $\mathbf{B}$: magnetic field strength, and E: total energy). The system of MHD equations is completed by the following equation of state:

$$P = (\gamma - 1)\left[E - \frac{1}{2}\rho V^2 - \frac{B^2}{8\pi}\right], \tag{2}$$

providing a frequently used thermodynamics relation to determine pressure. The vectors $\mathbf{F}$ and $\mathbf{G}$ in Eq. (1) are inviscid fluxes given by

$$\mathbf{F} = \begin{bmatrix} \rho V_x \\ P^* + \rho V_x^2 - B_x^2/4\pi \\ \rho V_x V_y - B_x B_y/4\pi \\ 0 \\ V_x B_y - B_x V_y \\ \rho V_x(E + P^*) - (\mathbf{B}\cdot\mathbf{V})\frac{B_x}{4\pi} \end{bmatrix}, \quad \mathbf{G} = \begin{bmatrix} \rho V_y \\ \rho V_x V_y - B_x B_y/4\pi \\ P^* + \rho V_y^2 - B_y^2/4\pi \\ V_y B_x - B_y V_x \\ 0 \\ \rho V_y(E + P^*) - (\mathbf{B}\cdot\mathbf{V})\frac{B_y}{4\pi} \end{bmatrix}, \tag{3}$$

where $P^* = P + B^2/8\pi$ is total pressure.

2.1. Quasilinear form and parameter state

The conservative form in Eq. (1) can be transformed into the following quasi-linear form (for clarity, assume $\mathbf{S} = 0$):

$$\frac{\partial \mathbf{U}}{\partial t} + A(\mathbf{U})\frac{\partial \mathbf{U}}{\partial x} + B(\mathbf{U})\frac{\partial \mathbf{U}}{\partial y} = 0 \tag{4}$$

provided that the linearized Jacobians (i.e., $A = \partial\mathbf{F}/\partial\mathbf{U}$ and $B = \partial\mathbf{G}/\partial\mathbf{U}$) are defined in terms of an appropriate average state, $\overline{\mathbf{U}}$. Since it is this quasi-linear form of the system of equations used by FS schemes,

the fluxes which are used in finite volume schemes are not estimated. See [32] for a comparison between the fluctuation splitting and finite volume schemes. Although it is not necessary to work in conservative variables in the derivation of the eigensystem of wave models in the FS schemes (see [25], for example), the flow variables (which are updated) are conservative variables in order to obtain correct weak solutions. The hyperbolic nature of this system gives rise to the following conservative matrix:

$$C_n = An_x + Bn_y, \tag{5}$$

which has real eigenvalues and a complete set of left and right eigenvectors for the vector, $\vec{n} = n_x\hat{e}_x + n_y\hat{e}_y$, that specifies the direction in which the disturbance in a physical quantity propagates as a wave.

In the FS scheme considered here, the values of physical quantities are stored at the vertices of a triangular mesh T whose area is S_T. During the time iterations, the resulting flux integral (or mesh fluctuation, $\mathbf{\Phi}_T$) is computed and distributed to the vertices of these meshes by means of an upwinding strategy. Since the MHD equations cannot be diagonalized, an approximate diagonalization method or so-called multidimensional wave model (see [6] for a review of Eulerian wave models) is used to specify such a distribution. The wave model allows the separation of mesh fluctuation into smaller parts (i.e., $\mathbf{\Phi}_T^\kappa$ associated with κth wave) in the mesh. Individual distribution of these wave fluctuations to the nodes is performed in such a way that overall conservation is retained (i.e., the relation $\mathbf{\Phi}_T = \sum_\kappa \mathbf{\Phi}_T^\kappa$ is always satisfied).

The time rate of the state vector $\mathbf{U}$ can be found by integrating Eq. (1) over the phase space i.e., triangular prism with a volume of $\Delta t S_T$ (where $\Delta t = t^{n+1} - t^n$ is time step)

$$\int_{t^n}^{t^{n+1}} \int\int_T \frac{\partial \mathbf{U}}{\partial t}\, \mathrm{d}S\, \mathrm{d}t = -\int_{t^n}^{t^{n+1}} \int\int_T (\mathbf{F}_x + \mathbf{G}_y)\, \mathrm{d}S\, \mathrm{d}t = \mathbf{\Phi}_T^*, \tag{6a}$$

$$= -\Delta t \left[\left[\int\int_T A\, \mathrm{d}S \right] \mathbf{U}_x + \left[\int\int_T B\, \mathrm{d}S \right] \mathbf{U}_y \right]^*, \tag{6b}$$

where the update is explicit when $\mathbf{\Phi}_T$ is evaluated at old time level (i.e., $* \to n$) or implicit when it is found at t^{n+1}. Because implementing implicit algorithms for unstructured triangular meshes is complicated, a multistage Runga–Kutta (RK) scheme is utilized in order to improve time accuracy [5]. Since it is unnecessary to stick with $\mathbf{U}$ to carry out the above spatial integrations, a parameter state vector, $\mathbf{Z}$, that is assumed to vary linearly over the mesh is utilized. The form of it can be determined (analytically) by requiring the elements of $\mathbf{U}$, $\mathbf{F}$, and $\mathbf{G}$ to be quadratic in their components of $\mathbf{Z}$. In this case, the resulting Jacobians $\mathbf{U}_z = \partial\mathbf{U}/\partial\mathbf{Z}$, $A_z = \partial\mathbf{F}/\partial\mathbf{Z}$, $B_z = \partial\mathbf{G}/\partial\mathbf{Z}$ will all be linear in terms of $\mathbf{Z}$ so that the area integrals will be realized by its mesh average: $\overline{\mathbf{Z}} = (\mathbf{Z}_1 + \mathbf{Z}_2 + \mathbf{Z}_3)/3$. When this procedure is followed, it can be found that such a parameter vector exists for the Euler system and is given by $\mathbf{Z} = \sqrt{\rho}(1, V_x, V_y, H)^{\mathrm{T}}$ where H is the enthalpy (see [2]). It is important to note that the use of this parameter state vector provides the Rankine–Hugoniot (RH) relations

$$\mathbf{F}_x + \mathbf{G}_y \equiv [A(\overline{\mathbf{Z}}), B(\overline{\mathbf{Z}})] \cdot (\mathbf{U}_x, \mathbf{U}_y) \tag{7}$$

to be satisfied over the triangular mesh.

Because of nonlinearity, it is impossible to derive such a parameter state for MHD so that some appropriate forms such as

$$\mathbf{Z} = \sqrt{\rho}\left(1, V_x, V_y, \frac{B_x}{\sqrt{\rho}}, \frac{B_y}{\sqrt{\rho}}, H\right)^{\mathrm{T}} \quad \text{or} \quad \mathbf{Z} = \sqrt{\rho}(1, V_x, V_y, B_x, B_y, H^*)^{\mathrm{T}} \tag{8}$$

(where $H^* = (E + P^*)/\rho$) can be used as demonstrated in [2]. In this work, the second option was considered. Although the exact solution of $\mathbf{Z}$ provides the discontinuity capture within one cell, using approximate parameter vectors causes the discontinuities to spread into a few cells. As it will be shown by

numerical results, the disadvantage of using an approximate parameter vector shows itself only in slightly spread contact discontinuities.

Using the property that $\mathbf{Z}$ is linear and hence its gradient, $\vec{\nabla}\mathbf{Z}$, is constant over T, the flux integral (or fluctuation) defined by Eq. (6b) becomes

$$\int\int_T \left(\frac{\mathbf{U}^{n+1}-\mathbf{U}^n}{\Delta t}\right) \mathrm{d}S = \mathbf{\Phi}_T^* = -\int\int_T (A\mathbf{U}_x + B\mathbf{U}_y)^* \,\mathrm{d}S, \tag{9a}$$

$$= -\left[\int\int_T (A\hat{e}_x + B\hat{e}_y)\mathbf{U}_z \,\mathrm{d}S\right]^* \cdot \vec{\nabla}\mathbf{Z}^*, \tag{9b}$$

$$= -S_T\left[A_z(\overline{\mathbf{Z}}), \mathbf{B}_\mathbf{z}(\overline{\mathbf{Z}})\right] \cdot \vec{\nabla}\mathbf{Z}^*. \tag{9c}$$

Note that since A_z and B_z are linear in Z, the following identities (with j being the nodes of T) were used in obtaining:

$$\frac{1}{S_t}\int\int_T (A_z, B_z)\,\mathrm{d}S = \left[\frac{1}{3}\sum_{j=1}^{3} A_z(\mathbf{Z}_j), \frac{1}{3}\sum_{j=1}^{3} B_z(\mathbf{Z}_j)\right] = \left[A_z(\overline{\mathbf{Z}}), \mathbf{B}_\mathbf{z}(\overline{\mathbf{Z}})\right]. \tag{10}$$

Thus, the fluctuation in Eq. (9a)–(9c) becomes

$$\Phi_T^* = -S_T\left[A(\overline{\mathbf{Z}})\hat{\mathbf{e}}_\mathbf{x} + \mathbf{B}(\overline{\mathbf{Z}})\hat{\mathbf{e}}_\mathbf{y}\right]^* \cdot \vec{\nabla}\mathbf{U}^*. \tag{11}$$

This shows that the matrix: C_n is evaluated in terms of $\overline{\mathbf{Z}}$ and that the average gradient: $\vec{\nabla}\mathbf{U}$ is found from $\vec{\nabla}\mathbf{U} = \mathbf{U}_z(\overline{\mathbf{Z}})\vec{\nabla}\mathbf{Z}$.

In the FS schemes, the total fluctuation (or the flux integral) in Eq. (11) is computed by the sum of the fluctuations due to the simple waves, whose physical properties are obtained analytically from C_n. The hyperbolic nature of the problem requires that the disturbances in density, momenta, and magnetic field convect by the nonlinear interaction of the waves propagating in the system. The gradients in flow quantities produced by these disturbances remain unchanged between the characteristic cones centered around the time axis, and they jump to different values as the surfaces of these cones (along which individual waves propagate) are crossed. This means that the gradient (i.e., x and y derivatives) of state variables can be projected onto a total of N right eigenvectors of $C_n(\overline{\mathbf{Z}})$

$$\vec{\nabla}\mathbf{U} = \sum_{\kappa=1}^{N} \vec{\nabla}\mathbf{U}^\kappa, \quad \vec{\nabla}\mathbf{U}^\kappa = \alpha_\kappa \mathbf{r}_n^\kappa \vec{n}^\kappa, \tag{12}$$

where α_κ is called the strength of κth wave and $\mathbf{r}_n^\kappa$ is its eigenvector. Using this result in Eq. (11), the total fluctuation can be written as the the sum of wave fluctuations

$$\Phi_T = \sum_{\kappa=1}^{N} \mathbf{\Phi}_T^\kappa, \tag{13}$$

where the wave fluctuation is given as

$$\mathbf{\Phi}_T^\kappa = -S_T\left[A\mathbf{U}_x + B\mathbf{U}_y\right]^\kappa = -S_T\left[(A\hat{e}_x + B\hat{e}_y)^\kappa \cdot \vec{\nabla}\mathbf{U}^\kappa\right], \tag{14a}$$

$$= -S_T[\alpha_\kappa(An_x + Bn_y)\mathbf{r}_n^\kappa] = -S_T[\alpha_\kappa C_n(\overline{\mathbf{Z}})\mathbf{r}_\mathbf{n}^\kappa], \tag{14b}$$

$$= -\mathbf{S}_\mathbf{T}[\alpha_\kappa \lambda_\mathbf{n}^\kappa \mathbf{r}_\mathbf{n}^\kappa] \tag{14c}$$

provided that λ_n^κ, satisfies the eigenvalue problem: $C_n\mathbf{r}_n^\kappa = \lambda_n^\kappa \mathbf{r}_n^\kappa$.

Notice that since all elements of C_n are evaluated in terms of $\overline{\mathbf{Z}}$, its eigensystem will be dependent on $\overline{\mathbf{Z}}$ while the wave-strengths and directions will be dependent on $\overline{\mathbf{Z}}$ and its gradient. Because this dependency is nonlinear, the differences in the form of $\mathbf{Z}$ as given in Eq. (8) will not cause significant changes in the numerical solutions (this is indeed verified by various numerical results).

Using the wave fluctuation given in Eq. (14c), and employing mass lumping (i.e., $\int\int \mathrm{d}S = \sum_{T\in i} S_T/3 = S_i$) the conservative time update of $\mathbf{U}_i$ located at the node i of T at the new time level $n+1$ becomes

$$\mathbf{U}_i^{n+1} = \mathbf{U}_i^n + \frac{\Delta t^n}{S_i} \sum_{T\in i} \left[\sum_{\kappa=1}^{N} D_{T,\kappa}^i \mathbf{\Phi}_T^{\kappa^*} + \frac{S_T}{3} S(\overline{\mathbf{Z}}) \right], \tag{15}$$

where S_i is median dual cell area around vertex i, $D_{T,\kappa}^i$ is the fraction of this fluctuation sent to node i in an upwind manner, and Δt is the time step satisfying the positivity constraint (i.e., $\Delta t = \sigma \min(\Delta x, \Delta y)/(|\vec{v}| + U_{\mathrm{F}})$), with σ, the CFL number.

2.2. Primitive form and wave model

The conservative fluctuation in Eq. (14c) is easily obtained by first writing MHD equations in terms of the primitive state, $\mathbf{W} = [\rho, V_x, V_y, B_x, B_y, P]^{\mathrm{T}}$:

$$\frac{\partial \mathbf{W}}{\partial t} + A_w(\overline{\mathbf{Z}})\mathbf{W}_{\mathbf{x}} + \mathbf{B}_{\mathbf{w}}(\overline{\mathbf{Z}})\mathbf{W}_{\mathbf{y}} = \mathbf{0}, \tag{16}$$

then finding the eigenvectors: $\mathbf{r}_w^\kappa$ of $C_w = A_w(\overline{\mathbf{Z}})\mathbf{n}_{\mathbf{x}} + \mathbf{B}_{\mathbf{w}}(\overline{\mathbf{Z}})\mathbf{n}_{\mathbf{y}}$, and finally using $\mathbf{r}^\kappa \equiv \mathbf{U}_w \mathbf{r}_w^\kappa$ where $U_w(\overline{\mathbf{Z}}) = \partial \mathbf{U}/\partial \mathbf{W}$ is the transformation matrix which satisfies $[\overline{A}_w, \overline{B}_w] = U_w^{-1}[\overline{A}, \overline{B}]U_w$. If the simple wave solution $\mathbf{W}(x, y, t) = \mathbf{W}(xn_x + yn_y - \lambda t)$ is inserted in Eq. (16), one gets $(\overline{A}_w n_x + \overline{B}_w n_y - \lambda I)d\mathbf{W} = 0$ stating that $d\mathbf{W}$ is an eigenvector of the matrix $C_w = \overline{A}_w n_x + \overline{B}_w n_y$ associated with the wave moving in the direction $\vec{n} = (n_x, n_y)$. This allows the following projection:

$$\vec{\nabla}\mathbf{W} = \sum_{\kappa=1}^{N} \alpha_\kappa \mathbf{r}_w^\kappa \vec{n}^\kappa \tag{17}$$

which can be used to derive the wavestrengths provided that x and y derivatives of $\mathbf{W}$ is known on T. The primitive matrix C_w for the planar MHD system considered in this work is the same as given in [2]. The eigenvalues of this matrix are given by

$$\Lambda_w = V_n, V_n, V_n - U_{\mathrm{S}}, V_n + U_{\mathrm{S}}, V_n - U_{\mathrm{F}}, V_n + U_{\mathrm{F}}, \tag{18}$$

where the first two represent the eigenvalues of entropy and artificial monopole waves and $V_n \pm U_{\mathrm{S}}$ and $V_n \pm U_{\mathrm{F}}$ represent the eigenvalues of the slow and fast magneto-acoustic waves, respectively. The slow and fast magneto-acoustic speeds are given by

$$U_{\mathrm{S/F}} = \left[\frac{1}{2} \left[a^2 + \frac{B^2}{4\pi\rho} \mp \left[(a^2 + \frac{B^2}{4\pi\rho})^2 - 4a^2 \frac{B_n^2}{4\pi\rho} \right]^{1/2} \right] \right]^{1/2},$$

where $a^2 = \gamma P/\rho$ is the square of the sound speed.

The primitive eigenvectors of C_w are given (in the same order of Λ_w) as the columns of the following matrix:

$$R_w = \begin{bmatrix} 1 & 0 & \rho & \rho & \rho & \rho \\ 0 & 0 & -r_{2S} & r_{2S} & -r_{2F} & r_{2F} \\ 0 & 0 & -r_{3S} & r_{3S} & -r_{3F} & r_{3F} \\ 0 & n_x & r_{4S}n_y & r_{4S}n_y & r_{4F}n_y & r_{4F}n_y \\ 0 & n_y & -r_{4S}n_x & -r_{4S}n_x & -r_{4F}n_x & -r_{4F}n_x \\ 0 & 0 & \rho a^2 & \rho a^2 & \rho a^2 & \rho a^2 \end{bmatrix}, \tag{19}$$

where

$$r_{2S/F} = [B_y U_{S/F} - \zeta_{F/S} \sin\theta]/B_\perp, \quad r_{3S/F} = [-B_x U_{S/F} + \zeta_{F/S} \cos\theta]/B_\perp,$$

$$r_{4S/F} = \frac{4\pi\rho}{B_\perp}(U_{F/S}^2 - \frac{B^2}{4\pi\rho}), \quad \zeta_{F/S} = \sqrt{4\pi\rho} a U_{F/S} \mathrm{sign}(B_n) \tag{20}$$

and $B_\perp = n_x B_y - n_y B_x$, the component of magnetic field perpendicular to $\vec{n}$.

As it was explained in [2], considering a total of 12 waves where the first set of 6 corresponding to the matrix $C_w^{\theta_1} = A_w n_{x1} + B_w n_{y1}$ and the second set corresponding to $C_w^{\theta_2} = A_w n_{x2} + B_w n_{y2}$, Eq. (17) becomes

$$\vec{\nabla}\mathbf{W} = \sum_{\kappa=1}^{6} \alpha_{\theta_1}^{\kappa} \mathbf{r}_{\theta_1}^{\kappa} \vec{n}_{\theta_1}^{\kappa} + \sum_{\kappa=7}^{12} \alpha_{\theta_2}^{\kappa} \mathbf{r}_{\theta_2}^{\kappa} \vec{n}_{\theta_2}^{\kappa}. \tag{21}$$

It can easily be seen from Eq. (21) that having 12 wave strengths and 2 different angles leads an overdetermined system of equations since there exists six x derivatives and six y derivatives on its left-hand side. In model MHD-A, the relation $\theta_2 = \theta_1 + \pi/2$ was chosen so that the extra magneto-acoustic waves would propagate in perpendicular directions (this idea was used earlier by Rudgyard [6] who developed Eulerian wave models). Thus, Eq. (21) becomes

$$\vec{\nabla}\mathbf{W} = (\mathbf{W}_x, \mathbf{W}_y) = \sum_{\kappa=1}^{6} \alpha_{\theta}^{\kappa} \mathbf{r}_{\theta}^{\kappa} \vec{n}_{\theta}^{\kappa} + \sum_{\kappa=7}^{12} \alpha_{\theta+\frac{\pi}{2}}^{\kappa} \mathbf{r}_{\theta+\frac{\pi}{2}}^{\kappa} \vec{n}_{\theta+\frac{\pi}{2}}^{\kappa}, \tag{22}$$

where $\vec{n}_\theta = n_x \hat{e}_x + n_y \hat{e}_y = \cos\theta \hat{e}_x + \sin\theta \hat{e}_y$, $\vec{n}_{\theta+\frac{\pi}{2}} = -\sin\theta \hat{e}_x + \cos\theta \hat{e}_y$.

Reducing the number of waves (and hence removing excess dissipation) is possible by combining two entropy (waves 1 and 7) and two monopole waves (waves 2 and 8) together. Allowing only two angles (θ_e for entropy and θ for other waves) and a total of 10 wavestrengths will then lead to the required 12 degrees of freedom. When these waves are combined, after some algebra one achieves the result

$$\alpha^1 \lambda^1 \mathbf{r}^1 + \alpha^7 \lambda^7 \mathbf{r}^7 = (\vec{\nabla}\rho - \vec{\nabla}P/a^2) \cdot \mathbf{V} = \alpha_e \lambda_e \mathbf{r}_e, \tag{23}$$

$$\alpha^2 \lambda^2 \mathbf{r}^2 + \alpha^8 \lambda^8 \mathbf{r}^8 = \alpha_m \lambda_m \mathbf{r}_m, \tag{24}$$

where $\lambda_e = V_x \cos\theta_e + V_y \sin\theta_e$, $\lambda_m = V_x \cos\theta + V_y \sin\theta$, and $\mathbf{r}_e$ and $\mathbf{r}_m$ are the eigenvectors located as the first and second columns of R_w given in Eq. (19). Thus, the total primitive fluctuation with 10 effective waves becomes

$$\mathbf{\Phi}_w^T = -S_T[A_w, B_w] \cdot \vec{\nabla}\mathbf{W}, \tag{25a}$$

$$= -S_T \left[\alpha_e^1 \lambda_e^1 \mathbf{r}_e^1 + \alpha_\theta^2 \lambda_\theta^2 \mathbf{r}_\theta^2 + \sum_{\kappa=3}^{6} \alpha_\theta^\kappa \lambda_\theta^\kappa \mathbf{r}_\theta^\kappa + \sum_{\kappa=7}^{10} \alpha_{\theta+\frac{\pi}{2}}^\kappa \lambda_{\theta+\frac{\pi}{2}}^\kappa \mathbf{r}_{\theta+\frac{\pi}{2}}^\kappa \right], \tag{25b}$$

where the subscripts e and m denote entropy and monopole waves and the last two sums represent the magneto-acoustic waves propagating in $\vec{n}_\theta$ and $\vec{n}_{\theta+\frac{\pi}{2}}$ directions, respectively. Note that since the updated variables are conservative ones, $\mathbf{\Phi}_w^T$ should be converted into the conservative fluctuation using $\mathbf{\Phi}_T = \mathbf{U}_w \mathbf{\Phi}_w^T$.

When solved analytically, the decomposition in Eq. (25b) results in the following relations for the wave-strengths (noting that the subscripts outside parenthesis denote the derivatives):

$$\alpha_{\mathrm{e}}^1 = \sqrt{[(\rho)_x - (P)_x/a^2]^2 + [(\rho)_y - (P)_y/a^2]^2}, \quad \alpha_{\mathrm{m}}^2 = \nabla \cdot \mathbf{B}, \tag{26a}$$

$$\alpha_{\mathrm{S}}^4 - \alpha_{\mathrm{S}}^3 = \frac{-U_{\mathrm{S}}}{2D}[\vec{\nabla} \cdot \mathbf{V} + V(\theta)] + \frac{\mathrm{sign}(B_n) U_{\mathrm{F}}}{D}\left[\frac{\Omega B_\perp + BV}{a\sqrt{4\pi\rho}}\right], \tag{26b}$$

$$\alpha_{\mathrm{S}}^4 + \alpha_{\mathrm{S}}^3 = \frac{B_\perp}{4\pi\rho}\left[\frac{\Omega_B + B(\theta)}{2D}\right] - \alpha_{\mathrm{s}} \frac{\vec{\nabla} P \cdot \vec{n}_\theta}{\rho a^2}, \tag{26c}$$

$$\alpha_{\mathrm{F}}^6 - \alpha_{\mathrm{F}}^5 = \frac{U_{\mathrm{F}}}{2D}[\vec{\nabla} \cdot \mathbf{V} + V(\theta)] - \frac{\mathrm{sign}(B_n) U_{\mathrm{S}}}{D}\left[\frac{\Omega B_\perp + BV}{a\sqrt{4\pi\rho}}\right], \tag{26d}$$

$$\alpha_{\mathrm{F}}^6 + \alpha_{\mathrm{F}}^5 = -\frac{B_\perp}{4\pi\rho}\left[\frac{\Omega_B + B(\theta)}{2D}\right] + \alpha_{\mathrm{f}} \frac{\vec{\nabla} P \cdot \vec{n}_\theta}{\rho a^2}, \tag{26e}$$

where $\Omega = (V_y)_x - (V_x)_y$ is the vorticity and other parameters are defined by: $D = U_{\mathrm{F}}^2 - U_{\mathrm{S}}^2$ and $BV = [(B_x(\mathbf{V})_x + B_y(\mathbf{V})_y)] \cdot \vec{n}_\theta$, $\Omega_B = (B_y)_x - (B_x)_y$, $\alpha_{\mathrm{f/s}} = (U_{\mathrm{F/S}}^2 - B^2/4\pi\rho)/D$, and

$$V(\theta) = \sin 2\theta[(V_y)_x + (V_x)_y] - \cos 2\theta[(V_y)_y - (V_x)_x],$$

$$B(\theta) = \sin 2\theta[(B_x)_x - (B_y)_y] - \cos 2\theta[(B_x)_y + (B_y)_x].$$

Note that the wave-strengths of the last four magneto-acoustic waves can be found from Eqs. (26b)–(26e) by interchanging $\vec{n}_\theta$ by $\vec{n}_{\theta+\frac{\pi}{2}}$ (i.e., $\cos\theta$ by $-\sin\theta$ and $\sin\theta$ by $\cos\theta$).

As it was shown in [2], the propagation direction of the entropy wave is the same as that of Euler system (model A of [1]) and that of the magneto-acoustic waves are in the direction of maximum magnetic strain

$$\tan\theta_{\mathrm{e}} = \frac{(\rho)_y - (P)_y/a^2}{(\rho)_x - (P)_x/a^2}, \quad \tan 2\theta = \frac{(B_x)_y + (B_y)_x}{(B_x)_x - (B_y)_y}. \tag{27}$$

It is interesting to observe that the magneto-acoustic angle is insensitive to velocity gradients, an important case which requires special treatment in the Euler limit.

2.3. Euler limit

It is important to obtain the correct Euler limit when the magnetic field vanishes (i.e., $\mathbf{B} \to 0$, so that $U_{\mathrm{F}} \to a$, $U_{\mathrm{S}} \to 0$, $\alpha_{\mathrm{f}} \to 1$, $\alpha_{\mathrm{s}} \to 0$). In this limit, the entropy system (λ^1, α^1, and $\mathbf{r}^1$) remains the same, magnetic monopole system vanishes and fast magneto-acoustic system turns into the two acoustic system of Euler equations:

$$\lambda^{5,6} = \mathbf{V}_n \mp a, \quad R_w^{5,6} = \left[\rho, \mp a\cos\theta, \mp a\sin\theta, 0, 0, \rho a^2\right]^{\mathrm{T}}, \tag{28a}$$

$$\alpha_{\mathrm{F}}^6 + \alpha_{\mathrm{F}}^5 = \frac{\vec{\nabla}P\cdot\vec{n}_\theta}{\rho a^2}, \quad \alpha_{\mathrm{F}}^6 - \alpha_{\mathrm{F}}^5 = \frac{1}{2a}\left[\vec{\nabla}\cdot\mathbf{V} + V(\theta)\right] \tag{28b}$$

moving with angle $\vec{n}_\theta$ and $\lambda^{9,10}$, $R_w^{9,10}$, and $\alpha_{\mathrm{F}}^{10} \mp \alpha_{\mathrm{F}}^9$ moving with angle $\vec{n}_{\theta+\frac{\pi}{2}}$. When forward and backward slow magneto-acoustic waves for θ and $\theta+\frac{\pi}{2}$ are combined and one takes $[\mathrm{sign}(B_n)/B_\perp] \to 1/4$, $[\mathrm{sign}(B_n)/B_\perp]_{\theta+\frac{\pi}{2}} \to 0$ in $r_{2\mathrm{S}}$, $r_{3\mathrm{S}}$ and those for $\theta+\frac{\pi}{2}$ given in Eq. (20), the shear wave of the Euler system is obtained

$$R_w^3\alpha^3 + R_w^4\alpha^4 + R_w^7\alpha^7 + R_w^8\alpha^8 = \frac{\Omega}{2}\left[0, -\sin\theta, \cos\theta, 0, 0, 0\right]^{\mathrm{T}} = \alpha_{\mathrm{shear}}R_{\mathrm{shear}}, \tag{29}$$

where Ω is the vorticity and the strength of the shear wave. Thus, these waves turn into the 6 waves of model A of [1]. These results show that model MHD-A reduces identically to Roe's model in the limit where magnetic fields vanishes. The only problem with this limit is that the magneto-acoustic wave propagation angle given in Eq. (27) does not include velocity gradients so that it is unable to reduce the Eulerian angle

$$\tan 2\theta = \frac{(V_y)_y - (V_x)_x}{(V_y)_x + (V_x)_y} \tag{30}$$

that was used in [1]. Although this angle can be activated in Euler limit by a suitable switching mechanism or by a careful averaging of two angles comparing $|\mathbf{V}|$ with $|\mathbf{B}|/\sqrt{4\pi\rho}$, it is still an open question whether it is possible to obtain a propagation angle which reduces identically to that given in Eq. (30). According to the numerical experience of the author, such switching produces excellent results in Euler limit as will be shown by numerical results.

Using the results obtained so far the conservative time update of $\mathbf{U}$ at the ith node of T can be written as

$$\mathbf{U}_i^{n+1} = \mathbf{U}_i^n - \frac{\Delta t^n}{S_i}\sum_{T\in i} S_T\left[\sum_{\kappa=1}^{10} D_{T,\kappa}^i\alpha_\theta^\kappa\lambda_\theta^\kappa r_\theta^\kappa - \frac{\mathbf{S}(\overline{\mathbf{Z}})}{3}\right]^*, \tag{31}$$

where the last term is the average source (i.e., external force, gravitational force, artificial sonic and monopole sources) which is equally distributed to the vertices of each triangle and $D_{T,\kappa}^i$ are distribution coefficients mentioned earlier.

The idea of upwinding is to assign the fluctuation due to the κth wave (Eq. (14c)) only to the nodes of T towards which it is traveling. In order to select the upwind nodes, the signs of the following distribution parameters are used

$$d_i^\kappa = \frac{1}{2}\vec{\lambda}_i^\kappa\cdot\hat{n}_i L_i, \tag{32}$$

where λ^κ is the κth eigenvalue of C_n, $\hat{n}_i$ are the inward normal vectors along the sides i whose lengths are L_i. The geometry requires that $\sum_{i=1}^3 \hat{n}_i L_i = 0$ and hence $\sum_{i=1}^3 d_i = 0$ stating that the signs of d_i cannot be the same. If the sign of d_i^κ is positive and those of others are negative, the node i is the upwind node. Therefore, the fluctuation due to wave κ, given by Eq. (14c), is assigned only to this node, resulting in the following distribution coefficients:

$$D_{T,\kappa}^i = 1, \quad D_{T,\kappa}^j, \quad D_{T,\kappa}^k = 0. \tag{33}$$

Otherwise, two nodes with positive distribution coefficients are upwind nodes for this wave and its fluctuation is individually distributed between these nodes. In this work, two types of distribution strategy are utilized (N and NN methods).

Let us assume that the nodes i and j are upwind nodes for the two node update. The first method is called positive and linearity preserving N scheme which produces narrowest discontinuities. In this scheme, the wave fluctuation, Φ_T^κ, is first decomposed into two components, i.e., $\Phi_T^\kappa(\vec{\lambda}^\kappa) = \Phi_i^\kappa(\vec{\lambda}_i^\kappa) + \Phi_j^\kappa(\vec{\lambda}_j^\kappa)$ since it is linear in $\vec{\lambda}^\kappa$ and then they are assigned to the nodes i and j, respectively. Notice that $\vec{\lambda}_i^\kappa$ and $\vec{\lambda}_j^\kappa$ are the projections of $\vec{\lambda}^\kappa$ along the sides across nodes i and j, respectively, see Fig. 1(a). These components are given by $\vec{\lambda}_i^\kappa = D_{T,\kappa}^i \vec{\lambda}^\kappa$, $\vec{\lambda}_j^\kappa = D_{T,\kappa}^j \vec{\lambda}^\kappa$ (with $D_{T,\kappa}^i + D_{T,\kappa}^j = 1$) where

$$D_{T,\kappa}^i = \frac{(\vec{n}_\theta \cdot \hat{n}_i L_i)(\vec{n}_\theta \cdot \vec{r}_{kj})}{2S_T}, \quad D_{T,\kappa}^j = \frac{(\vec{n}_\theta \cdot \hat{n}_j L_j)(\vec{n}_\theta \cdot \vec{r}_{ki})}{2S_T}, \quad D_{T,\kappa}^k = 0, \tag{34}$$

where $\vec{r}_{ki/j}$ are vectors pointing from vertex k to i/j. Thus, the fluctuation for these downwind nodes becomes

$$\Phi_i^\kappa(\vec{\lambda}_i^\kappa) = D_{T,\kappa}^i \Phi_T^\kappa \quad \text{and} \quad \Phi_j^\kappa(\vec{\lambda}_j^\kappa) = D_{T,\kappa}^j \Phi_T^\kappa \tag{35}$$

so that the conservation requirement is satisfied.

The second method used in this work is called NN (nonlinear narrow) scheme which is the same as N scheme except that the frontal speed in the distribution parameters is modified by: $\vec{\lambda}^* = \vec{\lambda} + \vec{\lambda}_s = \vec{\lambda} + c\hat{n}_s$ where $c = -\vec{\lambda} \cdot \hat{n}_s$ and $\hat{n}_s$ is the unit vector parallel to the isolines of $\mathbf{U}$, see Fig. 1(b). This modification does not alter the wave fluctuation since the unit vector in the gradient direction, $\hat{n}_G = \vec{\nabla}\mathbf{U}/|\vec{\nabla}\mathbf{U}|$, is perpendicular to $\hat{n}_s$ so that $\vec{\lambda}^* \cdot \vec{\nabla}\mathbf{U} = \vec{\lambda} \cdot \vec{\nabla}\mathbf{U}$. Thus, the distribution parameters for NN scheme become

$$d_i^\kappa = \frac{1}{2}\vec{\lambda}_i^* \cdot \vec{n}_i = \frac{1}{2}[(\vec{\lambda}_i \cdot \hat{n}_G)\hat{n}_G] \cdot \vec{n}_i = \frac{1}{2}\vec{\lambda}_G \cdot \vec{n}_i. \tag{36}$$

Since NN scheme takes the gradients into consideration, it can detect unphysical expansion shocks and mostly eliminate them as will be shown by numerical results.

With N or NN type distributions, the FS scheme described so far carries first order accuracy in space. The spatial accuracy of this scheme can be increased to second order by means of limiters through the nonlinear PSI scheme [6]. In PSI scheme, Φ_i^κ and Φ_j^κ which are given in Eq. (35) are modified as

$$\Phi_i^* = \Phi_i - L(\Phi_i, -\Phi_j), \quad \Phi_j^* = \Phi_j - L(\Phi_j, -\Phi_i), \tag{37}$$

where $L(x, y)$ is Minmod limiter [7] given by

$$L(x, y) = \frac{1}{2}(\text{sign}(x) + \text{sign}(y))\min(|x|, |y|). \tag{38}$$

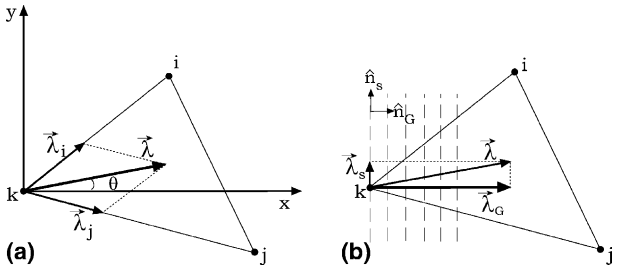

Fig. 1. The two node distribution of the fluctuation by N and NN methods.

2.4. Sources and sonic fix

The right-hand side of Eq. (1) includes external sources (such as gravitational force) as well as the artificial sources to cure problems associated with magnetic monopoles or unphysical expansion shocks. The numerical divergence source ($\mathbf{S}_{\text{div}}$) arises from inserting an artificial magnetic monopole wave into the eigensystem in order to eliminate undesired effects of non-physical magnetic monopoles (see [2] for details). In the work presented here artificial monopole wave is kept in the eigensystem but $\mathbf{S}_{\text{div}}$ is set to zero since its effects are negligible in comparison with the monopole wave's dissipation effects.

It is well known that most of the approximate Riemann solvers suffer from non-physical expansion shocks at sonic points where one of the eigenvalues changes its sign and becomes small or vanishes. If sonic points are not handled correctly, such algorithms may not converge to the entropy satisfying solutions. Some methods to treat sonic points have been developed by several investigators (see [3] for a review) and successful results had been obtained. In most of these sonic fixes, the eigenvalues are allowed to pass through sonic points smoothly so that the dissipation at sonic points does not vanish and that the second order accuracy is not reverted to the first order. Recently, the most striking sonic fixes were developed by Roe [8] for the Euler equations and by Aslan and Kammash [3] for the MHD equations. These authors realized that considering the rate of sonic gradients was the key issue for a physically correct sonic treatment. Roe suggested that the state around the sonic interface should have been modified to eliminate expansion shocks while Aslan showed that a pointwise dissipation which is directly embedded into the interface fluxes also produces a correct sonic treatment. In this work, Aslan's sonic treatment [3] was modified and adapted to the described FS scheme. Since the nodal update methodology of the FS schemes requires mesh averages and x and y derivatives of the state, before the nodal updates take place, this existing information can be used to detect if a mesh is likely to include a sonic point. If the magnitude of an eigenvalue nearly vanishes and it changes sign in any one of the neighboring triangles, its gradient is maximized. When this phenomenon is observed the associated mesh is flagged to include a sonic point. To get a correct sonic dissipation at this point, the system of equations are expanded in time by a higher order Taylor polynomial (see [3] for details) and the following second order sonic vector is obtained:

$$\mathbf{S}^{\text{sonic}} = -\frac{\Delta t}{2}\left[(A)_x(\mathbf{F})_x + (B)_y(\mathbf{G})_y\right] \tag{39}$$

to be equally distributed among the nodes of T as a regular source vector. Note that A_x and B_y are x and y derivatives of the Jacobian matrices defined in [2]. How this vector is obtained at sonic points can be easily understood if the procedure in [3] is followed for 2D. For example, it can be shown that Eq. (39) produces the following form of the sonic source for the x momentum:

$$S_{2,i}^{\text{sonic}} = -\frac{\Delta t S_i}{2S_T}(3-\gamma)(V_x)_x\left(\rho V^2 + P + \frac{B_y^2 - B_x^2}{8\pi}\right)_x + \mathrm{O}(\Delta x^3) \tag{40}$$

when the sonic interface is in the x direction. If this term is distributed equally among each node of T, the artificial pointwise dissipation applied to x-momentum will fix the sonic problem. By comparison with the results in [3] one can find that this term is related to the correct sonic gradient and that its magnitude decays exponentially in time while the sonic fix is being performed (this was actually shown in [3] and re-observed by the author).

3. Visual implementation

The visual capability of VIS-MHD-A was established by using specially written visualization subroutines (of Graphical-User-Interface, GUI) all of which are designed to work in parallel (as multi-threaded) with the computations. This property allows us to analyze the features of the calculated quantities at any time and on any spatial point in the solution domain (to obtain a demo version of this code see [9]). The graphical interface was developed such that the code can be modified so that it can be run in parallel on a network of workstations (see [4]). The user friendly code, VIS-MHD-A, was developed such that structured meshes (for simple geometries) or unstructured meshes (for complex domains) can be produced and appropriate boundary conditions can be specified interactively by the user before the simulation starts. In addition, desired flow features (including color and vector graphics as well as PIC type motion trajectory) and mesh structure can be visualized on the screen. During the time iterations, the GUI collects the nodal values, evaluates averages, and converts them into 50 different colors for the high resolution color image display. Only one set of vectoral quantities is stored on a typical mesh for vector graphics. The color and vector graphics updates on the screen are carried out by GUI at a certain frequency specified by the user. Although the data communication for graphical and the data processing by GUI causes a minor slowdown during the iterations, it is not of practical importance since the graphing frequency is usually chosen to be very low for time dependent problems. Since the graphs of the solutions are important only at the end of the steady state iterations, GUI graphics are only utilized at the end of iterations and therefore cause no corresponding slowdown. The vector graphics are used to visualize the online changes in the velocity and magnetic fields and color graphics are used to visualize scalar quantities such as density, pressure, and Mach number. In addition to the vector and color graphics options, the user can also analyze the solution profiles along the horizontal and vertical directions meeting at a point created by left and right mouse

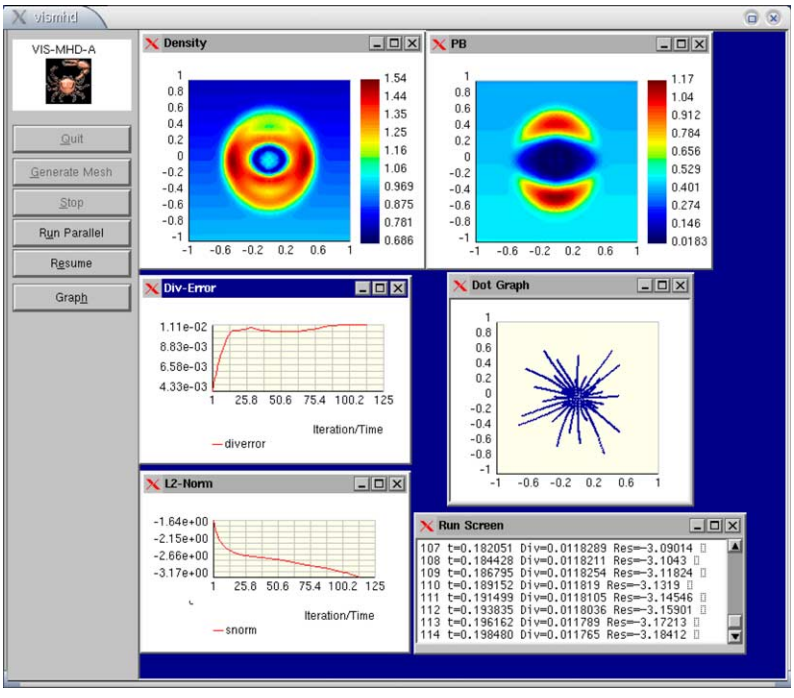

Fig. 2. A typical screen view displayed by GUI during a sample run.

clicking. The creation of a structured/unstructured grids, the selection of solver type and test problems with appropriate input parameters, and the intervention of graphical features are all user-friendly. Pausing the runs to take the snapshots of the visual features, restarting and stopping the executions can all be done by means of the GUI. Although the visual part of the code is continuously being improved, a typical page running a sample test is shown in Fig. 2. The details of the visualization features of VIS-MHD-A can be found in [10].

4. Numerical results

To test the validity of VIS-MHD-A described up to this point, some previously published one and two dimensional test problems were solved on a variety of structured and unstructured meshes. The first set of tests were carried out on highly elongated (in x direction) triangular grids to check the codes performance in the one dimensional limit. The second set which were run on Cartesian grids of different size included two dimensional tests which covered a wide range from subsonic to compressible flow regimes.

4.1. One dimensional tests

For a numerical method designed to investigate shock and discontinuity dynamics, it is necessary to test its properties by initiating nonlinear waves arising from an initial discontinuity and following their propagation. This can easily be established by checking if the code passes a variety of one or more dimensional tests previously studied. In order to check the performance of VIS-MHD-A in one dimensional limit, a set of test problems including shocks, contact discontinuities, rarefaction waves, and compound waves were solved on a rectangular domain, $[0,1]$, covered by highly elongated (in x direction) 200, 800, 1600×3 right running diagonal triangles. To initiate the runs, the x-axis is divided into two equal halves on which left and right states are defined to initiate different nonlinear MHD waves. The outgoing boundary conditions (where the boundary nodes are untouched) were used on all boundaries and the results were obtained before the fastest waves arrive at the left and right boundaries.

4.1.1. Test 1: Sod's shock tube test ($\gamma = 1.4$)

This famous hydrodynamic test that was first introduced in [11] involves a left moving fast rarefaction (FR−), a right moving contact discontinuity (CD+) and a fast shock (FS+). The initial data (with $\mathbf{B} = 0$) were chosen as $\mathbf{W}^{\mathrm{L}} = [1,0,0,0,0,1]$, $\mathbf{W}^{\mathrm{R}} = [0.125,0,0,0,0.1]$ and the problem was run until $t = 0.411$. The resulting density and V_x profiles in x direction (as a function of different mesh sizes) are shown in Fig. 3. As seen, the solution shows no post-shock oscillations and the contact and shock get sharper as the mesh resolution is increased, see [12] for the comparison of this result with previous ones. This result shows that model MHD-A reduces to the correct 1D limit as magnetic field vanishes. No efforts were taken to set magnetic field and V_y to zero, although some negligible errors for these fields were observed near the shock and contact. Note that these errors get smaller as the mesh is made finer.

4.1.2. Test 2: strong sonic test ($\gamma = 5/3$)

This test, first introduced in [13], was chosen to show how the new sonic fix (described in Section 2.4) and the NN method are able to eliminate unphysical expansion shocks, a phenomenon from which most approximate Riemann solvers suffer. In this problem, the initial tangential field includes a jump but normal field B_x is zero, i.e., $\mathbf{W}^{\mathrm{L}} = [1,0,0,0,\sqrt{4\pi},1000]$, $\mathbf{W}^{\mathrm{R}} = [0.125,0,0,-\sqrt{4\pi},0.1]$. The problem (which includes and FR−, CD+, FS+) was solved on a 400×3 mesh with right running triangles and the resulting density and V_x profiles in x direction at $t = 0.003$ are shown in Fig. 4. This figure involves the solutions obtained with no sonic fix, with new sonic fix, and with the NN distribution scheme. As seen, the sonic fix does its job

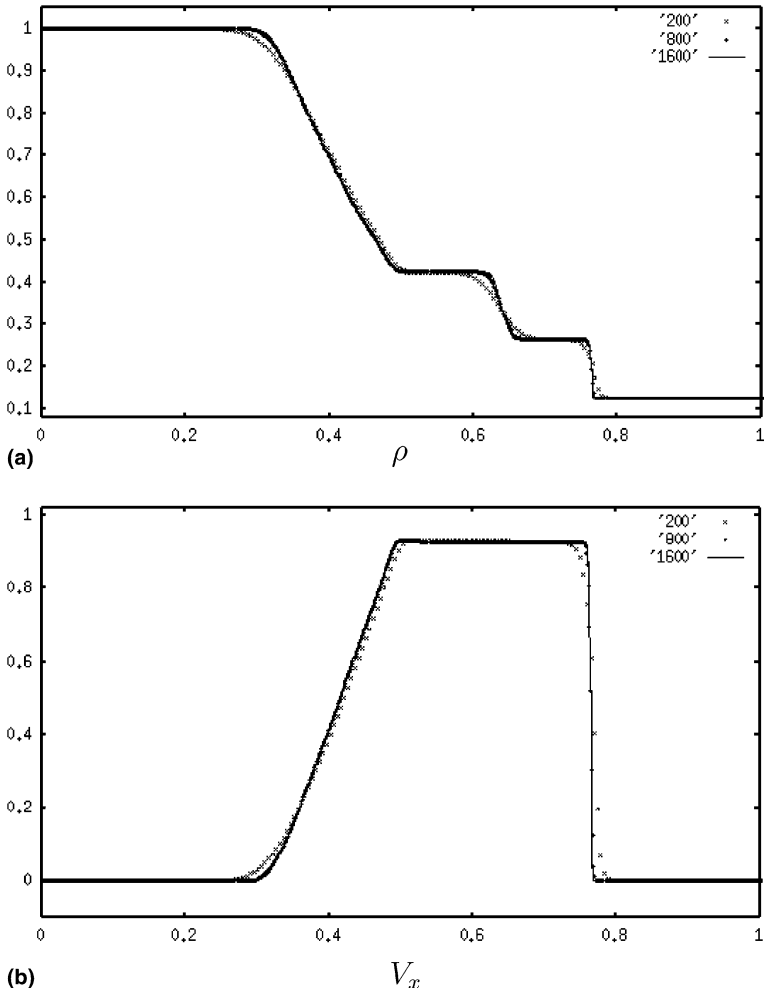

Fig. 3. Sod's shock tube test at on $t = 0.411$, 200, 800, 1600×3 R-grid, $\gamma = 1.4$. Plots show FR−, CD+, FS+ from left to right.

and eliminates expansion shock while NN method automatically handles the sonic problem with no fix required.

4.1.3. Test 3: slow shock and rarefaction test ($\gamma = 5/3$)

This test which can be found in [14] was chosen to see how sharp the slow shocks (SS) and how smooth the slow rarefactions (SR) will be, and if there exists post-shock oscillations due to slowly moving shocks. The initial data which includes a discontinuous tangential field are given by: $\mathbf{W}^{\mathrm{L}} = [1, 0, 0, 3, 5, 1]$, $\mathbf{W}^{\mathrm{R}} = [0.1, 0, 0, 3, 2, 10]$. The resulting density, pressure, V_x, and B_y profiles at $t = 0.08$ obtained on a 800×3 grid are presented in Fig. 5. The solution includes FS−, SR−, CD−, SR+, and FR+ from left to right. As seen, there are no post-shock oscillations, but contact and slow shock are spread over about 10–15 cells. This is expected since there is extra dissipation in the scheme (produced by extra waves added to the wave model), the parameter state is approximate, and the slow shock is very weak. However, these discontinuities become sharper when the mesh size is reduced.

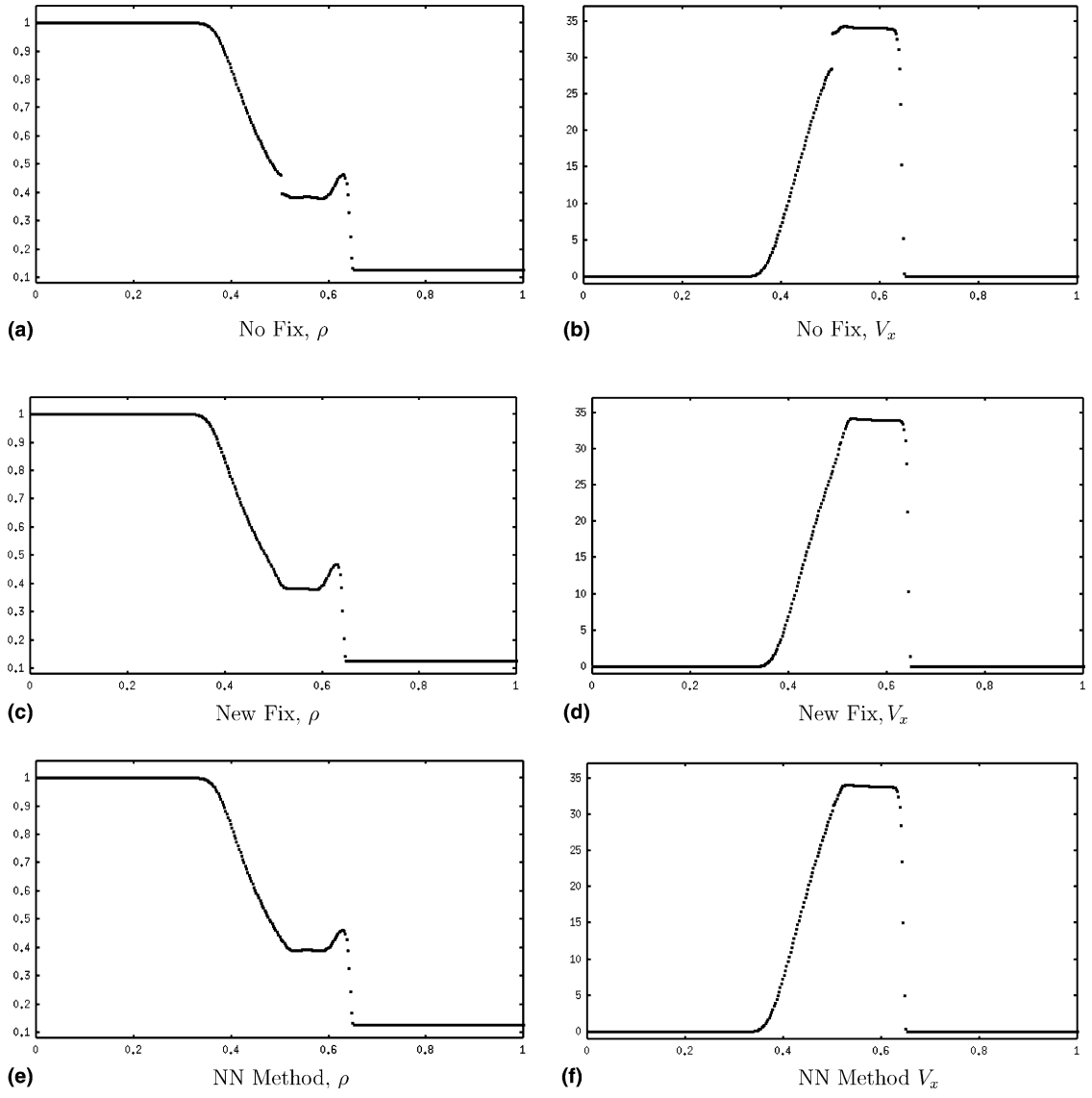

Fig. 4. Strong sonic test at $t = 0.003$, on 400×3 grid, $\gamma = 5/3$. Plots show FR−, CD+, FS+ from left to right.

4.1.4. Test.4: switch-on shock problem ($\gamma = 5/3$)

This test that can be found in [14] was chosen to examine how the scheme described here deals with switch-on fast shocks (SO-FS) behind which the tangential field turns on. The initial left and right state values are given as

$$\mathbf{W}^{\mathrm{L}} = [1, 0, 0, \sqrt{4\pi}, \sqrt{4\pi}, 1], \quad \mathbf{W}^{\mathrm{R}} = [0.2, 0, 0, \sqrt{4\pi}, 0, 0.1].$$

The resulting profiles (at $t = 0.15$) shown in Fig. 6 include FR−, SR−, CD+, SS+, and SO-FS+. As seen, the tangential field turns on behind SO-FS+ successfully; however, there exists a small undershoot on the top of the slow rarefaction wave. Yet also another observation is that although it is weaker, slow shock is sharper

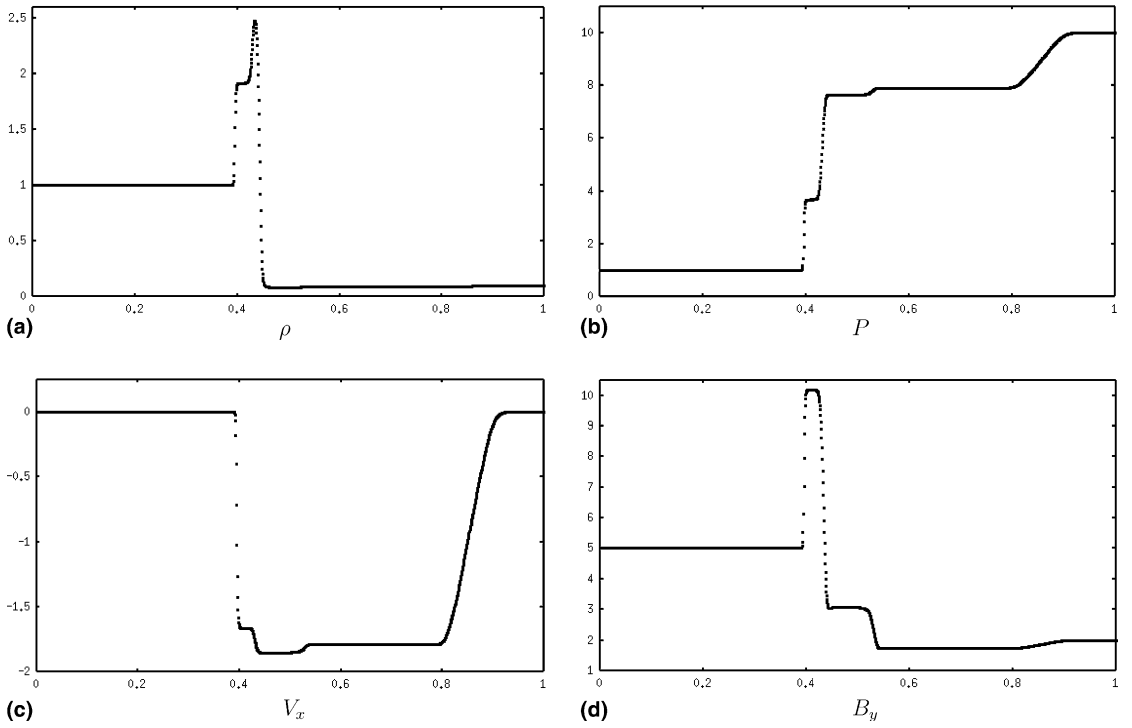

Fig. 5. Slow shock and rarefaction test at $t = 0.03$, 800×3 grid, with $\gamma = 5/3$. Plots show FS−, SS−, CD−, SR+, FR+ from left to right.

than the fast shock. This shows that the code treats equally to the slow and fast shocks in terms of their sharpness determined by the strength of the shock. Note that these results agree very well with the results presented in [14].

4.1.5. Test 5: compound wave test ($\gamma = 5/3$)

This test was first introduced in [15] and it involves compound waves (CW) originating from structures involving a shock and the rarefaction of the same wave family moving together. The initial data are such that the tangential magnetic field changes sign across the initial discontinuity

$$\mathbf{W}^{\mathrm{L}} = [1, 0, 0, 0.75\sqrt{4\pi}, \sqrt{4\pi}, 1], \quad \mathbf{W}^{\mathrm{R}} = [0.125, 0, 0, 0.75\sqrt{4\pi}, -\sqrt{4\pi}, 0.1].$$

The resulting field profiles at $t = 0.1$ obtained on a 800×3 grid are presented in Fig. 7. The solution includes both left and right running fast rarefactions (FR−, FR+), left running slow compound (SCW−), and right running contact (CD+) and a slow shock (SS+) waves. The fact that VIS-MHD-A is able to solve this test accurately is very interesting since the MHD equations considered here are planar (i.e., $v_z = 0, B_z = 0$) so that the Alfven wave is inexistent in the eigensystem, unlike the case in [15]. This shows that, although the Alfven wave structure is not explicitly included in model MHD-A, the dissipation that are produced by magneto-acoustic waves gives rise to this compound wave structure, resulting in correct physics.

All of the above one dimensional shock tube tests show agreement between the analytical solutions and previously published results. The positions and strengths of the shocks, rarefactions, and contact discontinuities are correct and there exists no post-shock oscillations. Further work can be done to steepen

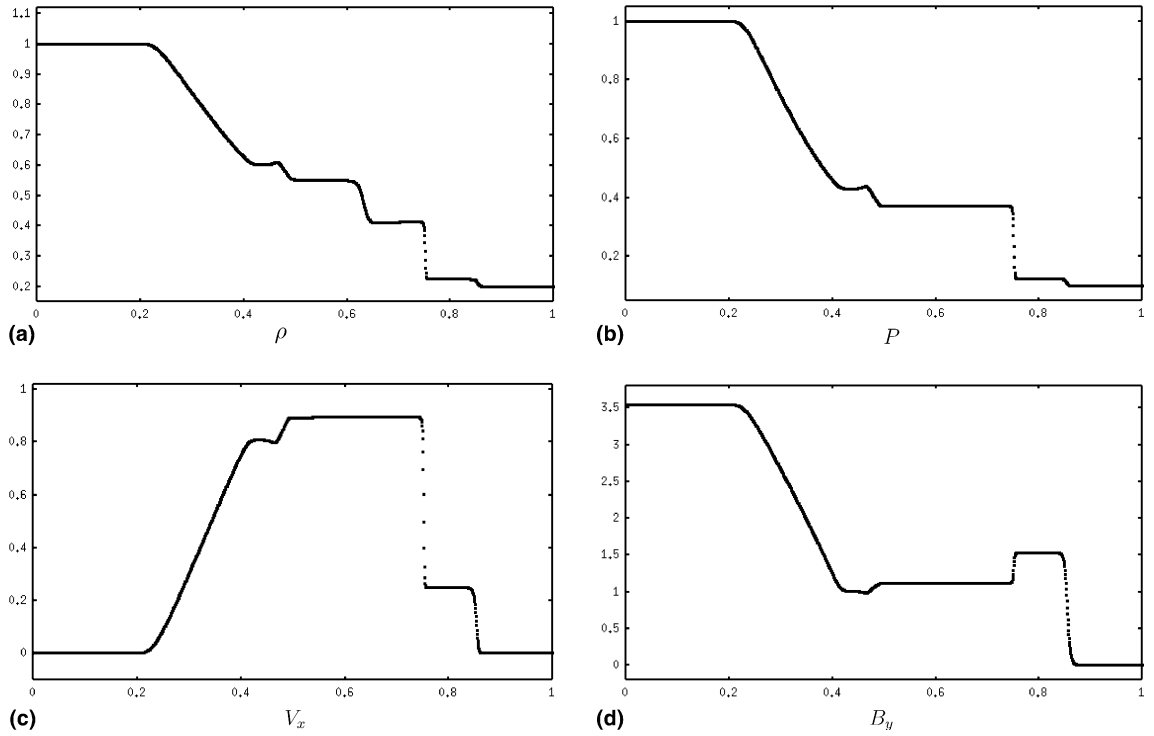

Fig. 6. Switch on fast shock test, at $t = 0.15$, 800×3 grid, with $\gamma = 5/3$. Plots show FR−, SR−, CD+, SS+, SO-FS+ from left to right.

contact discontinuities and slow shocks to improve the discontinuity capturing ability of the code VIS-MHD-A.

4.2. Two dimensional tests

The excellent performance of the code for two dimensional tests will be shown in this section. These tests were all performed on a Cartesian grid with isotropic triangles of different size. All the images of the physical quantities presented were obtained by taking the colorful image snapshots of the screen of VIS-MHD-A during the actual time iterations and saving them as colorful or gray scaled images. These tests include steady and unsteady problems, which cover a wide range from subsonic to supersonic and hypersonic flow regimes. In all of these tests, the CFL number was set to 0.4 and the problems were run by the third order RK algorithm [5].

4.2.1. Test 1: MHD shock reflection test, Euler limit (Mach = 2.9)

This purely hydrodynamic test, with $\gamma = 1.4$, was performed on a rectangular domain of $[0, 3.6] \times [0, 1]$ which was covered by isotropic triangular meshes involving 220×60 nodes. See Fig. 8(a) for a typical isotropic grid.

The left boundary was taken to be a supersonic inflow boundary (on which all state values were specified) and the upper boundary values were taken analytically to initialize a Mach = 2.9 flow with a reflected shock from the lower boundary. On this boundary, reflection boundary condition was imposed (where only V_y was forced to vanish and other state quantities were untouched) and the right boundary was considered to be outgoing (nodal values untouched). The initial condition was chosen to be the same as the left

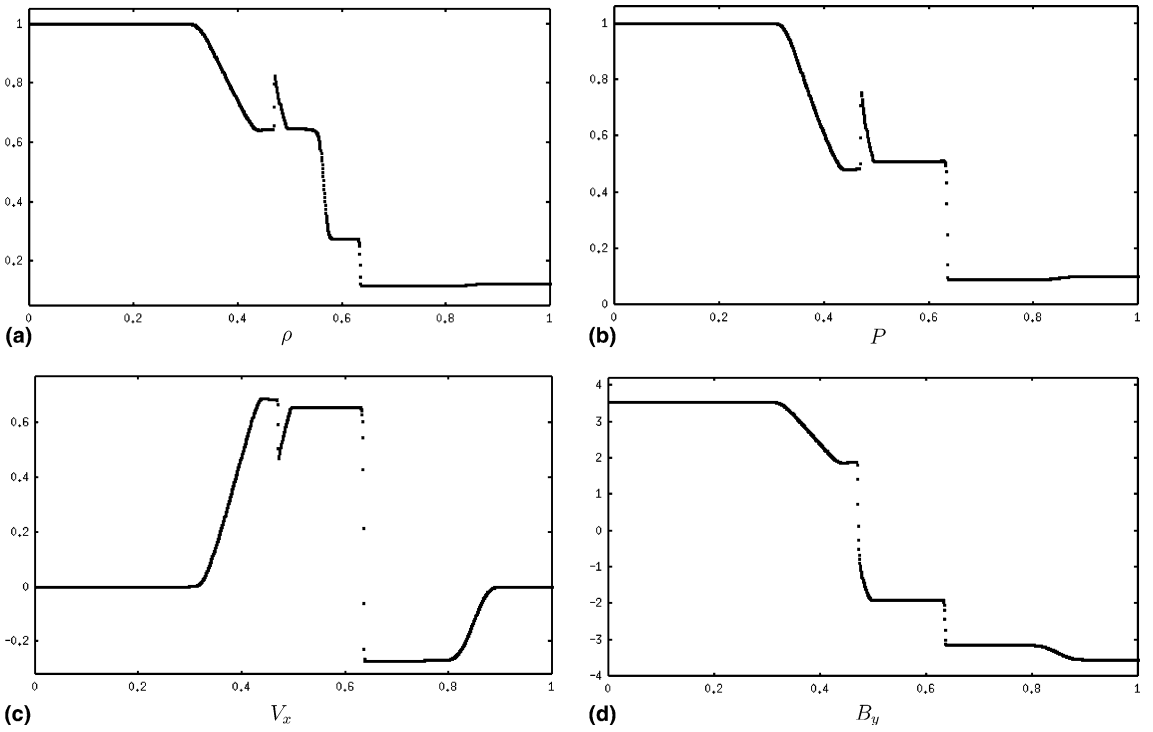

Fig. 7. Compound wave test, at $t = 0.1$, 800×3 grid, $\gamma = 5/3$. Plots show FR−, CW−, CD+, SS+, FR+ from left to right.

boundary condition. The boundary conditions are given by $\mathbf{W}^{\text{init}} = \mathbf{W}^{\text{left}} = [1, 2.9, 0, 0, 0, 1/\gamma]$, $\mathbf{W}^{\text{upper}} = [1.7, 2.6193, -0.5063, 0, 0, 1.5282]$ so that the steady state solution is a 23° reflected supersonic shock. This problem was run (using Euler angle in Eq. (30)) until the density residual dropped to 10^{-11}. During the runs, the magnetic fields were left untouched even though small deviations from zero were observed near discontinuities. The resulting density image obtained at $t = 4$ is shown in Fig. 8(b).

When the solutions for physical quantities were examined closely, it was found that the density, pressure, V_x and V_y assume the values of 2.6843, 2.9343, 2.4024, 0.0008, respectively, past the reflected shock. These results are in excellent agreement with the analytical results (i.e., 2.68732, 2.93413, 2.40148, 0) which were given in [31]. This agreement shows that VIS-MHD-A is able to handle the 2D-Eulerian limit successfully provided that the Eulerian angle given in Eq. (30) is utilized.

4.2.2. Test 2: MHD shock reflection test (Mach = 2.9)

This is the MHD version of Test 1 which was originally introduced by the author in [2]. The following boundary conditions were used to produce a steady state reflected supersonic and subalfvenic shock $\mathbf{W}^{\text{init}} = \mathbf{W}^{\text{left}} = [1, 2.9, 0, \sqrt{\pi}, 0, 1/\gamma]$, $\mathbf{W}^{\text{upper}} = [1.46, 2.717, -0.405, 2.424, -0.361, 1.223]$. This problem was run on different isotropic grids of 21×5, 41×11, 81×21, 161×41 on a rectangular domain of $[0, 4] \times [0, 1]$. For these meshes, the maximum divergence errors were evaluated from

$$\text{DIV}_{\max} = \left(\sum_{\text{mesh}} |\vec{\nabla} \cdot \mathbf{B}| \right) \left(\sum_{\text{mesh}} \frac{|B_x|_{\min} + |B_y|_{\min}}{\Delta x_{\max} + \Delta y_{\max}} \right)^{-1} \tag{41}$$

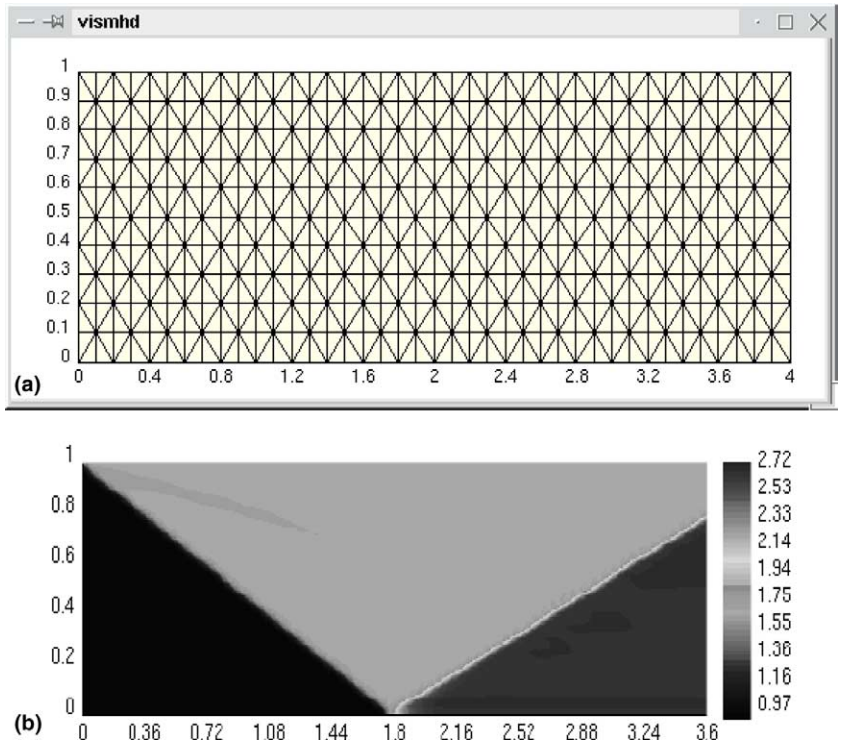

Fig. 8. (a) A typical isotropic grid used in shock reflection tests. (b) Oblique shock reflection test: steady state density image on isotropic 220×60 grid, $\gamma = 1.4$.

as done in [2,16] and they are plotted as a function of time in Fig. 9. As seen from Fig. 9, the maximum divergence error is nearly halved as the mesh resolution is doubled and the errors tend to reduce in time. These magnetic flux convergence results show that the artificial monopole wave in extended model MHD-A is able to reduce the errors due to nonzero divergence of the magnetic fields. In order to show the grid convergence in the solutions, the x-profiles of the density at $y = 0.5$ were plotted in Fig. 9(b) as a function of different grid sizes. The result is that the reflected shock is as sharp as the incident shock and shocks converge to correct locations as the grid resolution is increased.

4.2.3. Test 3: Orszag–Tang vortex (Mach = 1)

This problem (with $\gamma = 5/3$) considers an astrophysical MHD vortex and serves as an excellent test to check if the MHD models can successfully represent the evolution of turbulence, see [17,18]. The initial velocity and magnetic fields are

$$\mathbf{V} = -\sin(2\pi y)\hat{e}_x + \sin(2\pi x)\hat{e}_y, \quad \mathbf{B} = -\sqrt{4\pi}\sin(2\pi y)\hat{e}_x + \sqrt{4\pi}\sin(4\pi x)\hat{e}_y$$

and initial density and pressure are 2.777 and 1.587, respectively. Thus, the plasma beta: $\beta = P_0/B_0^2/8\pi$ and Mach number: $M = V_0/\sqrt{\gamma P_0/\rho}$ assume the values of 10/3 and 1, respectively. This initial configuration includes a central x-point at which the velocity and magnetic fields vanish. This problem was solved on a variety of isotropic triangular meshes of $[0,1] \times [0,1]$ and periodic boundary conditions were used at all boundaries in order to map the toroidal problem onto the Cartesian plane. The resulting snapshots of density, pressure, magnetic pressure: $B^2/8\pi$, and kinetic energy: $(1/2)\rho V^2$ at $t = 3$ obtained on a high

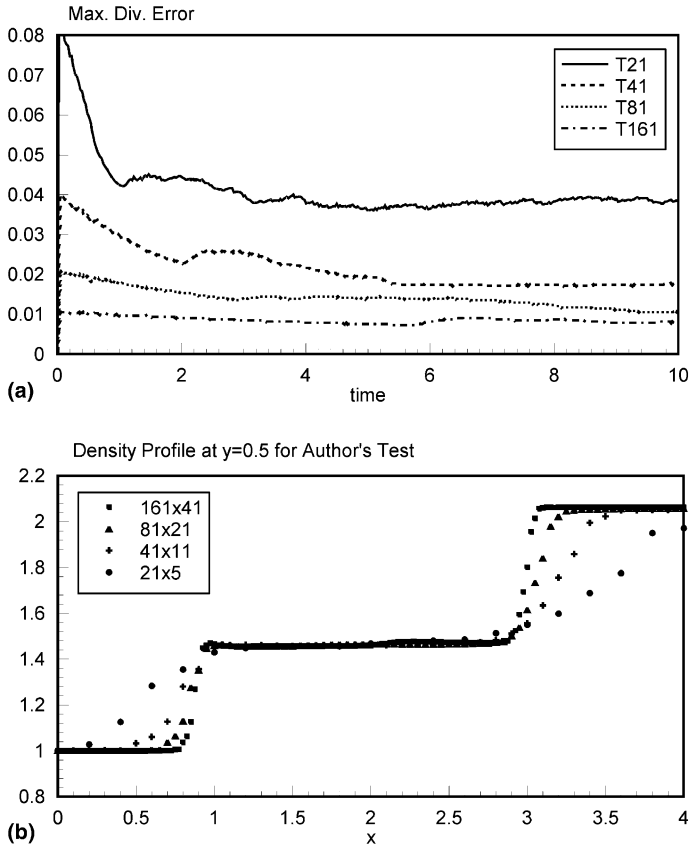

Fig. 9. (a) The time rate of maximum divergence error as a function of different grid sizes for author's shock reflection test. (b) The density profiles (at $y = 0.5$) as a function of different grid sizes for author's shock reflection test.

resolution 255×255 isotropic grid are shown in Fig. 10(a). The thermal pressure profile (with a cut at $y = 1/3.23$) was plotted at $t = 3.1$ in Fig. 10(b) to study the convergence properties of the scheme and to compare the results with those given in [18] in which a 192×192 square mesh and a total variation diminishing flux corrected scheme were used. It is seen that as the mesh is made finer, the agreement with [18] becomes excellent since the contacts and shocks are sharp and located correctly, and the dynamics of the x-point at the center is preserved correctly. This result shows that VIS-MHD-A produces a correct decay of the vortex system by its numerical viscosity and resistivity built in its wave model by means of a number of wave dissipations.

4.2.4. Test 4: hypersonic shock–cloud interaction

This problem (which was first introduced in [19]) deals with the disruption of a superfast high density circular cloud while passing by a strong shock. The problem was solved on a square Cartesian grid of $[0, 1]$ with isotropic triangles of a total of 121×121 nodes.

The strong shock was produced by considering different states (suitable with the RH conditions) on both sides of the shock surface located at $x = 0.6$. The states on the left and right side of initial discontinuity are given as: $\mathbf{W}^{\mathrm{L}} = [3.86, 0, 0, 0, 2.18, 167.35]$, $\mathbf{W}^{\mathrm{R}} = [1, -11.25, 0, 0, 0.56, 1]$. The dense cloud with a radius of 0.15 centered at $x = 0.8$, and $y = 0.5$ on the right side was produced by taking 10 times greater density so

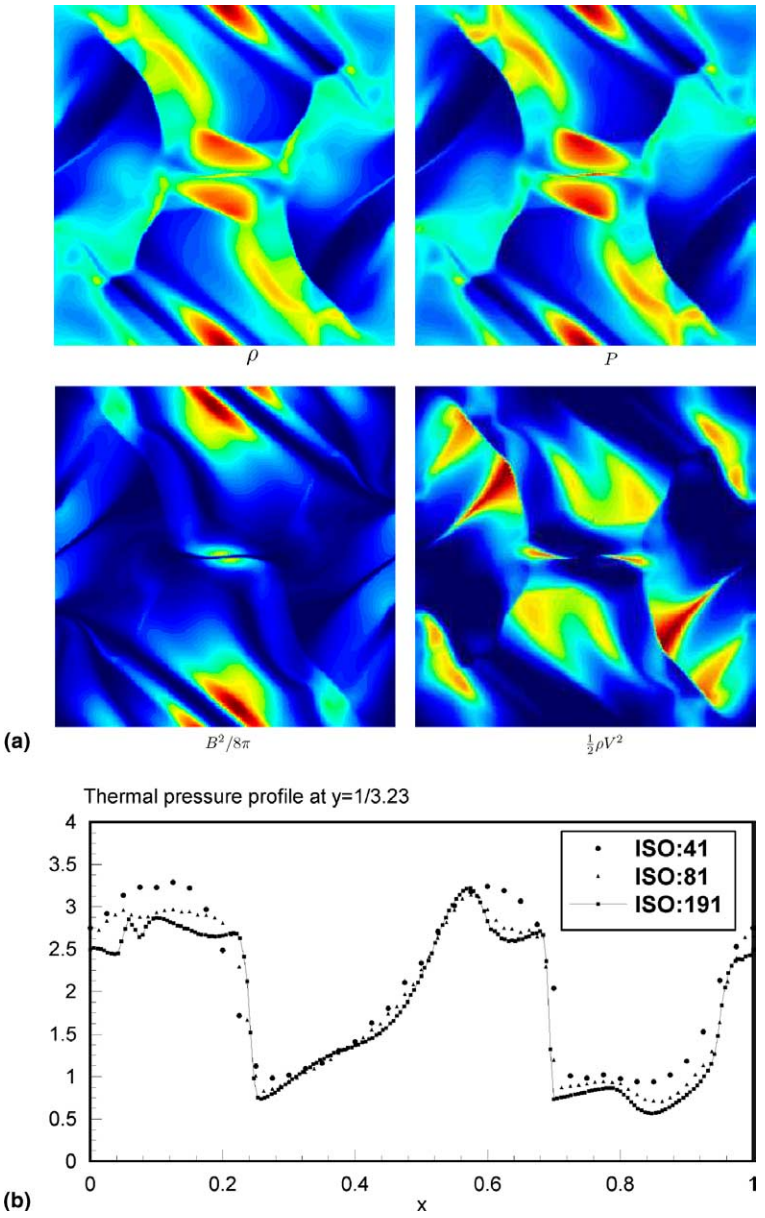

Fig. 10. (a) Orszag–Tang vortex test on 255×255 grid, $\gamma = 5/3$. Plots show the images of density, pressure, magnetic pressure, $B^2/8\pi$, and kinetic energy, $(1/2)\rho V^2$ at $t = 3$. (b) The thermal pressure profile obtained at $t = 3.1$ and at $y = 1/3.23$ for 41×41, 81×81, and 191×191 isotropic grids.

that the cloud moves towards the shock surface with a speed of Mach = 28. It is noted that the initial conditions used in this work are the same as those given in [19] except that no z fields are considered here. The resulting density, pressure, plasma beta, $\beta = P/(B^2/8\pi)$, and magnetic pressure images at $t = 0.06$ are shown in Fig. 11. As seen from this figure, the shock surface is bent and after passing the shock surface, the circular shape of the cloud is destroyed (with a denser head region) and a high pressured bow shock is

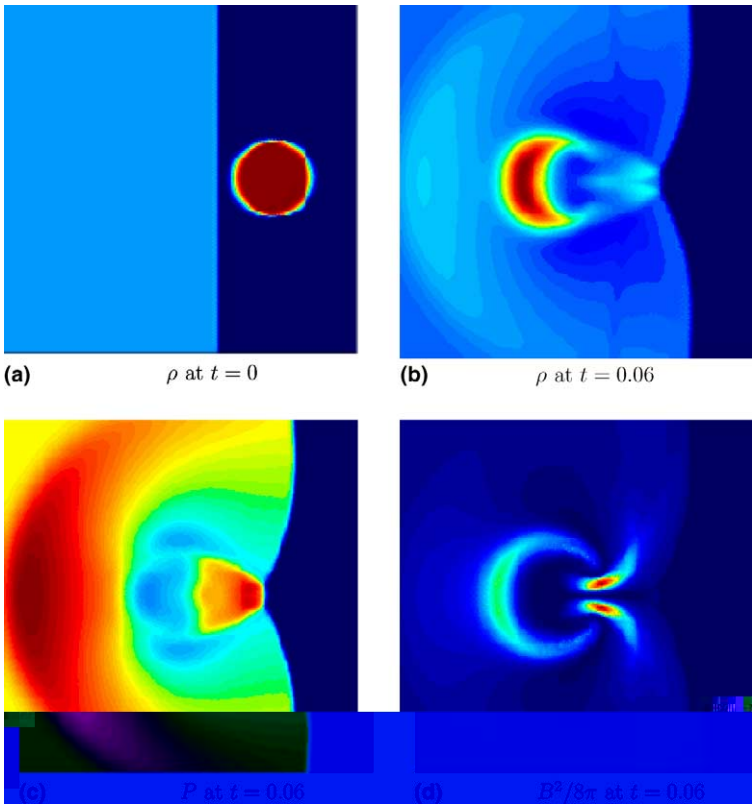

Fig. 11. Hypersonic shock–cloud test on 120×120 grid, $\gamma = 5/3$. Plots show the images of initial density, and the density, pressure, and magnetic pressure, $B^2/8\pi$ at $t = 0.06$.

produced ahead. It is evident from this expected result that VIS-MHD-A is able to handle such high Mach number flows including strong shocks.

4.2.5. Test 5: bow shock test

This problem represents a steady bow shock produced by a supersonic flow around a cylinder (see [20] for a similar test) and it was chosen to represent the convergence properties of the scheme running on unstructured meshes. Fig. 12 shows four different rectangular grids of $[0,4] \times [0,4]$ with a central circle generated by the unstructured grid producing algorithm of VIS-MHD-A. The initial conditions were taken as $\rho = 1$, $P = 0.2$, $V_x = 2$, $B_x = 0.1\sqrt{(}4\pi)$ to produce supersonic and super Alfvenic flow around the circle. The left inflow boundary was taken to be the same as initial conditions, the normal velocity around the circle boundary was taken as zero, and the other boundaries were taken as free boundaries in order to allow a free outflow.

As seen from Fig. 13, the divergence errors reduce by increased grid resolution and increased number of nodes around the circle. This grid convergence study shows that the monopole source in the wave model also works very well for unstructured meshes. The resulting density and pressure images obtained on the high resolution grid (Fig. 12) are shown in Fig. 14. Although the solution presented in [20] includes the domain in front of the circle, the solutions presented here includes the backward flow part in addition to agreeing with the previous solution.

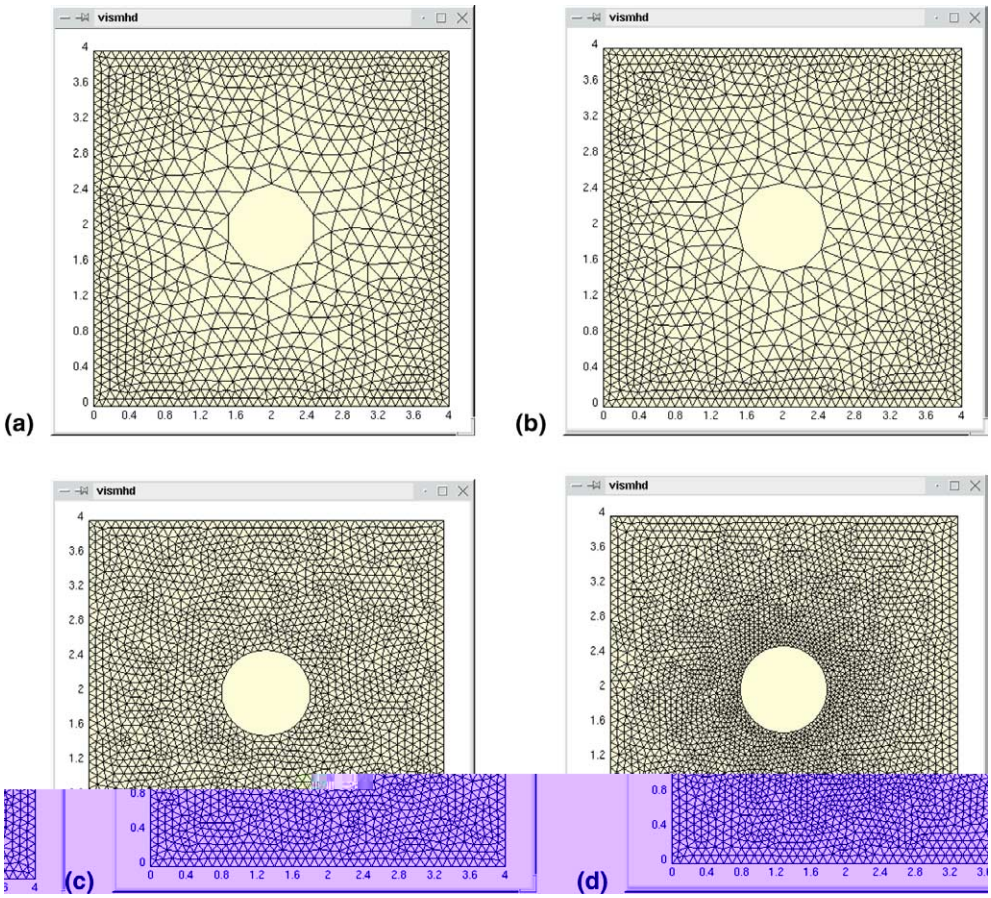

Fig. 12. Different unstructured meshes for the convergence study of bow shock test. The node numbers are 1028, 1129, 2161, 2908 from (a) to (d).

4.2.6. Test 6: Rayleigh–Taylor instability

This 2D test is the Rayleigh–Taylor (RT) instability that occurs when a heavy fluid is supported by a lighter fluid in a gravitational field. This instability (observed in supernova explosion, in accretion onto magnetospheres of neutron stars, in laser fusion, and many other contexts) was studied analytically by Chandrasekhar [21], and experimentally by other scientists, see [22] for a review. During the initial phase of this instability, exponentially growing perturbations cause penetration of the heavy fluid into the lighter one in a finger shape and the rising up of the lighter fluid. As the RT fingers grow, the relative motion between the two fluids drives secondary Kelvin–Helmholtz (KH) instability, turning the tips of the fingers into a mushroom shape,and eventually the fingers brake and the turbulent stage begins. Linearized theory suggests that the horizontal magnetic field can suppress this instability. If the densities of heavy and light fluids are given by ρ_{H} and ρ_{L}, the minimum critical value of this field to suppress RT instability is given by, see [21]

$$B_T^{\mathrm{cr}} = \frac{\sqrt{2\pi g/k(\rho_{\mathrm{H}} - \rho_{\mathrm{L}})}}{\cos\theta}, \tag{42}$$

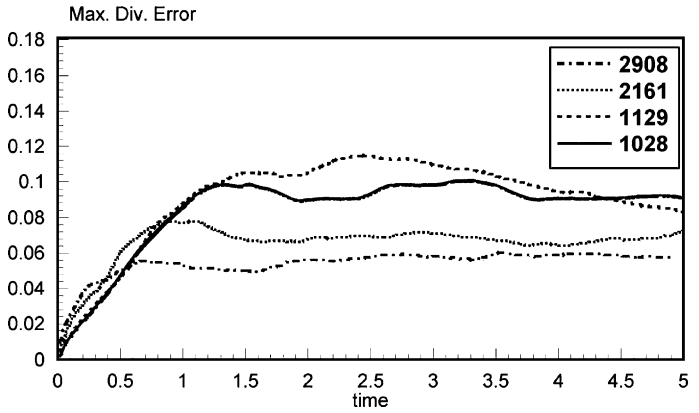

Fig. 13. The numerical error of $\nabla \cdot \mathbf{B}$ error convergence study for bow shock test.

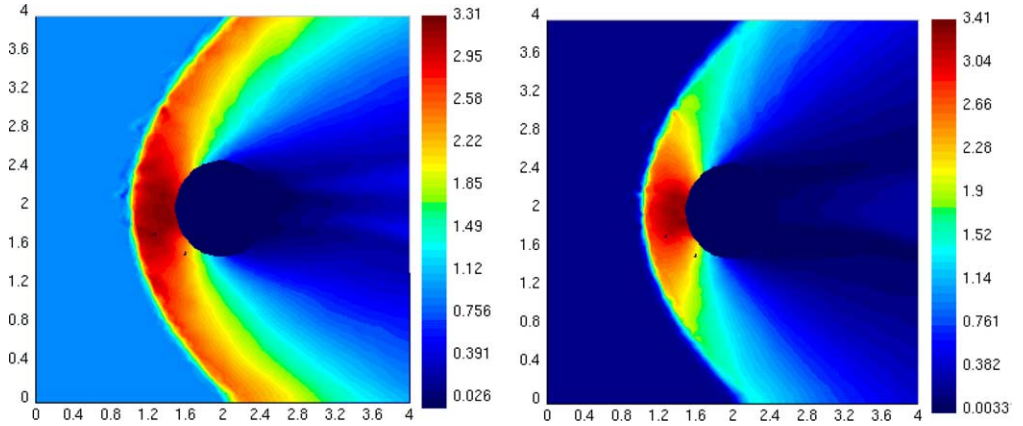

Fig. 14. The density and pressure images for the bow shock test obtained on the unstructured mesh (of Fig. 12(d)) including 2908 nodes.

where g is the acceleration due to gravity, k is the wave number of the initial perturbation, and θ is the angle between the magnetic field and wave vector. In order to check the performance of the code for this problem, a Cartesian isotropic grid of $[0,4] \times [-3,1]$ was taken and the initial interface between heavy and light fluids was considered to be located at $y = 0$. Initially, $\rho_{\mathrm{H}} = 20,\ \rho_{\mathrm{L}} = 1,\ P = 1,\ g = 0.1$ was taken (with $\gamma = 1.4$) and the following velocity perturbations which drive four fingers were considered, see [23]

$$V_x = 0.25 \sin(2\pi x) \mathrm{e}^{-2\pi|y|}(2H_y - 1), \quad V_y = 0.25 \cos(2\pi x) \mathrm{e}^{-2\pi|y|}, \tag{43}$$

where $H_y = 1$ for $y > 0$ and $H_y = 0$ otherwise. When initial magnetic field is taken in x direction (i.e., $\theta = 0°$ and $k = \pi/2$) is considered, the critical magnetic field is found to be 2.757 from Eq. (42). Fig. 15 displays the density contours at five different times as a function of the horizontal magnetic field strength. The columns from left to right denote the times $t = 1$ to $t = 5$ and the rows from top to bottom denote increased horizontal magnetic field strength: $B_x = 0.5$, $B_x = 1$, $B_x = 2$, $B_x = 2.757$, $B_x = 4$, $B_x = 6$, respectively. As seen from the top figures in Fig. 15, the instability takes place for this weak magnetic field, the bubbles occur in

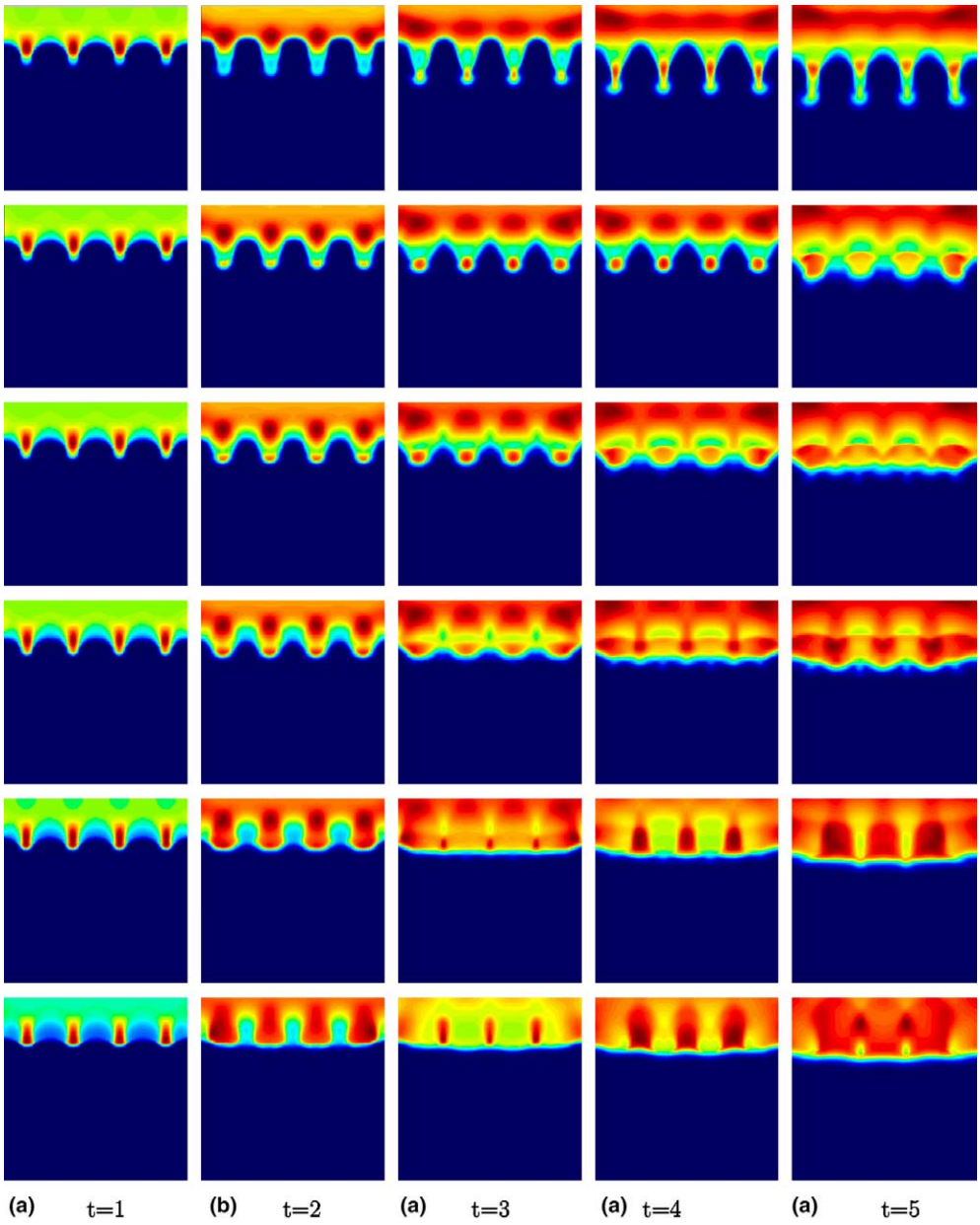

Fig. 15. RT Instability test density images at different times as a function of horizontal magnetic field strength. The values of B_x change from top to bottom as 0.5, 1, 2, 2.757, 4, 6, respectively.

heavy fluid between fingers, and finally mushroom type structures are produced at the tips. These results show that the code is able to produce results agreeing with the theory in (almost) pure hydrodynamics limit. When the strength of this magnetic field is increased, the growth of the fingers start to cease at $B_x = 2.757$ and the interface is stabilized for stronger fields. Notice that in all cases, the interface moves downward very slowly due to the weak gravitational force. These results agree very well with the theory as demonstrated.

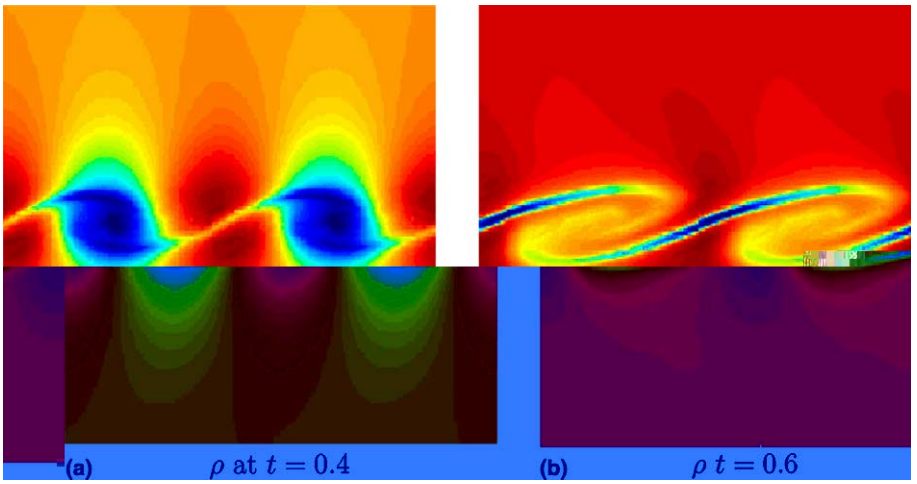

Fig. 16. Kelvin–Helmholtz test on 100×200 grid, $\gamma = 1.4$. Plots shows the images of density at $t = 0.4$ and $t = 0.6$.

4.2.7. Test 7: Kelvin–Helmholtz (KH) instability

This problem was chosen to check if VIS-MHD-A can handle low Mach number, conducting shear flows in the presence of magnetic fields. The flow was characterized by initial constant density ($\rho = 1$), pressure ($P = 50$), horizontal magnetic field ($B_x = B_0\sqrt{4\pi}$), a hyperbolic horizontal velocity: $V_x = V_0 \tanh(20y)$, and a perturbed perpendicular velocity: $V_y = 0.25\sin(2\pi x)e^{-100y^2}$ along with $\gamma = 1.4$. This problem was solved on a Cartesian grid of $x \in [0,1], y \in [-1,1]$ with 101×201 isotropic triangles with outgoing top and bottom boundaries and periodic left and right boundaries. With this given form, the horizontal velocity (V_0 at $y = 1$) changes sign across a shear surface located at $y = 0$ and reaches $-V_0$, resulting in maximum initial change of $2V_0$. The instability will be suppressed only if this change is smaller than initial Alfven velocity (i.e., $U_A = \sqrt{B_0^2/\rho}$). Fig. 16 gives the density images at $t = 0.4$ and $t = 0.6$ for $V_0 = 5$, and $B_0 = 1$. As seen, since the magnetic field is not sufficiently strong to suppress instability, a vortex (rotating clockwise) emerges and mixes the fluids around the initial shear layer. This solution, which compares well with that given in [24], shows that VIS-MHD-A again does an excellent job for such a subsonic shear flow.

All these two dimensional and one dimensional test results show that VIS-MHD-A can efficiently be used for steady state or time dependent simulation of neutral and charged fluids from subsonic to hypersonic flow regimes.

5. Conclusion

The purpose of developing VIS-MHD-A was to provide the plasma physics community with a robust, accurate and user-friendly visual computer code to numerically solve two dimensional MHD flows. VIS-MHD-A operates with a fluctuation splitting scheme originally developed by Aslan [2] for structured or unstructured triangular meshes. This scheme includes a wave model, MHD-A, whose physical properties are analytically obtained from the eigensystem of flux Jacobians. The code does not utilize fluxes, and does not employ any dimensional or Strang-type splitting in time. Instead, it evaluates and distributes fluctuations in the triangular cells by means of a compact (and conservative) second order scheme requiring no information from neighbor cells. For such a distribution, first the propagation angles and the strengths of the waves (originating from the hyperbolic nature of MHD equations) are determined in triangular cells. Then, these waves are allowed to interact non-linearly in such a way that the shock-capturing property is

established in an accurate manner. The code is able to utilize explicit time stepping or higher-order multistage Runga–Kutta algorithms [5]. The code was designed to solve the MHD equations along with a possible external source such as external gravity, heat conduction, radiative cooling, etc. Since VIS-MHD-A solves ideal MHD equations, the viscosity and resistivity are automatically built into the wave model in order to produce numerical dissipation. The divergence condition in the magnetic field is handled by convecting and dissipating the artificial monopole wave that is allowed to move with the flow. How to handle the $\vec{\nabla} \cdot \mathbf{B}$ constraint by means of such a monopole wave was first addressed by Aslan [12] in his thesis and this idea was then used by Powell [26] to obtain rotated MHD problems in two dimensions. Since then, many investigators have been following this idea, although some others have been preferring to use constraint transport of Evans and Hawley [16] or projection scheme of Brackbill and Barnes [27], or the vector potential formalism (see [33,34] for a review). Nevertheless, it was observed by this author during numerous numerical examples that the monopole wave idea originally introduced by Aslan [12] works well for transient and steady state MHD problems in the range from subsonic to supersonic (and hypersonic) MHD flows (see [28,29]). An important feature of the code is its user-friendly visualization capability. With this code, structured or unstructured grids can be created by specifying domain boundaries, the color images of scalar quantities and vector plots of vectoral quantities can be displayed on screen, and a fast PIC algorithm can be used to follow the trajectories of the particles. This code is currently being extended to include partially ionized multi-species hypersonic plasma flows and their associated instabilities, see [30].

Acknowledgements

The partial support from NATO Collaborative Studies Programme is appreciated.

References

[1] P.L. Roe, Fluctuations and signals, a framework for numerical evolution problems, in: K.W. Morton, M.J. Baines (Eds.), Numerical Methods for Fluid Dynamics II, Academic Press, New York, 1982.
[2] N. Aslan, MHD-A: a fluctuation splitting wave model for planar magnetohydrodynamics, J. Comput. Phys. 153 (1999) 437–466.
[3] N. Aslan, T. Kammash, Numerical fluxes with new sonic fix for MHD equations, J. Comput. Phys. 133 (1997) 43–55.
[4] E. Onbasioglu, N. Aslan, A. Erdogan, PV-MHD-A: A Parallel and Visual CFD Code, National High Performance Computing Symp., Gebze Inst. of High Tech. Istanbul, Turkey, October 24–25, 2002.
[5] C.W. Shu, Total-variation-diminishing time discretizations, SIAM J. Sci. Stat. Comput. 9 (1988) 1073.
[6] M. Rudgyard, Multidimensional wave decompositions for the Euler equations, Computational Fluid Dynamics, von Karman Institute for Fluid Dynamics LS 1993-04, 1993.
[7] N. Aslan, Numerical solutions of one-dimensional MHD equations by a fluctuation approach, Int. J. Numer. Meth. Fluids 22 (1996) 569–580.
[8] P.L. Roe, Sonic flux formulae, SIAM J. Sci. Stat. Comput. 13 (2) (1992) 611–630.
[9] To receive a limited version of VIS-MHD-A, send e-mail to: naslan@yeditepe.edu.tr.
[10] N. Aslan, E. Onbasioglu, A. Erdogan, PV-MHD-A: a parallel and visual 2D-magnetohydrodynamics code, Int. J. Numer. Meth. Fluids (submitted 2004).
[11] G.A. Sod, Numerical Methods in Fluid Dynamics, Cambridge University Press, Cambridge, UK, 1985.
[12] N. Aslan, Computational investigations of ideal MHD plasmas with discontinuities, Ph.D. Thesis, University of Michigan, Nuclear Eng. Dept. USA, 1993.
[13] A. Zachary, P. Colella, A higher order Godunov method for the equations of ideal MHD, J. Comput. Phys. 99 (1992) 341–347.
[14] D. Ryu, T.W. Jones, Numerical magnetohydrodynamics: algorithm and tests for one-dimensional flow, Astrophys. J. 442 (1995) 228–258.
[15] M. Brio, C.C. Wu, An upwind differencing scheme for the equations of ideal MHD, J. Comput. Phys. 75 (1988) 400–422.
[16] C.R. Evans, J.F. Hawley, Simulation of magnetohydrodynamic flows: a constrained transport method, Astrophys. J. 332 (1988) 659–677.

[17] J. Michael Picone, R.B. Dahlburg, Evolution of the Orszag–Tang vortex system in compressible medium. II. Supersonic flow, Phys. Fluids 3 (1991) 29–44.
[18] G. Toth, D. Odstrcil, Comparison on some flux corrected transport and total variation diminishing numerical schemes for hydrodynamics and magnetohydrodynamics, J. Comput. Phys. 128 (1996) 82.
[19] W. Dai, P.R. Woodward, A high-order Godunov type scheme for shock interactions in ideal magnetohydrodynamics, SIAM J. Sci. Comput. 18 (1997) 957.
[20] H. De Sterck, A. Csik, D. Vanden Abeele, Stationary two-dimensional MHD flows with shocks: characteristic analysis and grid convergence study, J. Comput. Phys. 166 (2001) 28–62.
[21] S. Chandrasekhar, Hydrodynamic and Hydromagnetic Stability, Oxford University Press, Oxford, 1961.
[22] Y.M. Wang, N. Nepveu, A numerical study of the nonlinear Rayleigh–Taylor Instability, with application to acreting X-ray sources, Astron. Astrophys. 118 (1983) 267–274.
[23] A. Nichiguchi, T. Yabe, Second order fluid particle scheme, J. Comput. Phys. 32 (1983) 390–413.
[24] A. Malagoli, G. Bodo, R. Rosner, On the nonlinear evolution of magnetohydrodynamic Kelvin–Helmholtz instabilities, Astrophys. J. 456 (1996) 708–716.
[25] P.L. Roe, D.S. Balsara, Notes on the eigensystem of magnetohydrodynamics, SIAM J. Appl. Mech. 56 (1996) 57.
[26] K.G. Powell, An approximate Riemann solver for MHD (that works in more than one dimension), ICASE Report No. 94-24, Langley, VA, 1994.
[27] J.U. Brackbill, D.C. Barnes, The effect of nonzero $\vec{\nabla} \cdot \mathbf{B}$ on the numerical solution of the magnetohydrodynamic equations, J. Comput. Phys. 35 (1980) 426–430.
[28] N. Aslan, T. Kammash, A Riemann solver for two dimensional MHD equations, Int. J. Numer. Meth. Fluids 25 (1997) 1–5.
[29] N. Aslan, Two dimensional solutions of MHD equations with an adapted Roe Method, Int. J. Numer. Meth. Fluids 23 (1996) 1211–1222.
[30] M. Mond, I.M. Ruthkevich, Spontaneous acoustic emission from strong ionizing shocks, J. Fluid Mech. 275 (1994) 121–146.
[31] J. Giannakouros, G. Karniadapis, A spectral element-FCT method for compressible Euler equations, J. Comput. Phys. 115 (1994) 65–85.
[32] W.A. Wood, W.L. Kleb, On multi-dimensional unstructured mesh adapdation, AIAA Papers 99-3254, June 28, 1999.
[33] G. Toth, The $\operatorname{div} B = 0$ constraint in shock-capturing magnetohydrodynamics codes, J. Comput. Phys. 161 (2000) 605–652.
[34] P. Londrillo, L. Del Zanna, Higher order upwind schemes for multidimensional magnetohydrodynamics, Astrophys. J. 530 (2000) 508.